USE OF ABSORPTION LASER-INDUCED BREAKDOWN SPECTROSCOPY IN CHARACTERIZATION OF ACTINIDE SPECIES AND OXIDES

BY

EMILY NELUM WEERAKKODY

THESIS

Submitted in partial fulfillment of the requirements
for the degree of Master of Science in Mechanical Engineering
in the Graduate College of the
University of Illinois at Urbana-Champaign, 2018

Urbana, Illinois

Advisor:

Professor Nick Glumac

ABSTRACT

Spectroscopy in its many utilities presents the ability to remotely sense species present in potentially hazardous conditions. Of recent interest is the development of technologies to detect the presence of actinide materials, a group of radioactive species typically used in the manufacture of nuclear devices. Current spectral databases are incomplete with regard to less-studied materials, such as the actinide group. In order to assist in the development of this technology, the spectral signatures of these materials need to be found and catalogued.

Laser-induced breakdown spectroscopy (LIBS) is a commonly-used method to observe the spectra of materials in plasma conditions. This technique was used in conjunction with absorption spectroscopy, which provides the ability to determine concentration. Tests were performed on two samples, a pure Uranium sample, and an alloy of U_3Si_2, in order to determine changes in spectral signatures when ablated in various environments of different composition and pressure. The Uranium sample was first tested in varying concentrations of O_2, N_2, and Ar to observe changes in U I and U II species signatures. It was then tested targeting the UO transition at 593.55 nm to observe trends with ambient O_2 concentration, pressure, laser power, and spatial location in plasma. The U_3Si_2 sample was tested to observe and compare temporal changes in U I, U II, Si I, UO, and SiO species signatures.

For those who have supported me.

ACKNOWLEDGEMENTS

There are many who deserve acknowledgement for their impact on my research, education, and life. To name a few:

First and foremost, I would like to thank Professor Nick Glumac for affording me the opportunity to work in the Laser Diagnostics and Energetic Materials Research Laboratory at the University of Illinois. When I first started working for this group three and a half years ago, I did not know the first thing about being an experimentalist or what the process of research and discovery truly entailed. Under his guidance, I have grown greatly as a researcher and student and cannot begin to convey how grateful I am to him.

The admittedly tough journey that is research is made easier by being in good company. I would like to thank Christopher Murzyn, Jose Guadarrama, and Chee Haw Chan for teaching me valuable skills, helping me overcome obstacles, and inspiring me to continue the journey to graduate school. I would also like to thank my compatriots Brian Read, Rylie Lodes, Nick Poirier, Dave Amondson, Joel Schwallier, Larsson Johnson, and Daniel Meaney for always being willing to teach, brainstorm, and assist when the need arises. I would additionally like to thank postdoc Adam Sims for always being generous with his expertise, as well as our awesome undergraduate students for always being willing to help, notably Alexandra Baumgart.

I like to thank David Weisz and Mike DeMagistris for their helpful collaboration over the course of my master's, and I am grateful to Professor Emeritus Herman Krier for his invaluable advice and for proofreading this document.

I would like to thank my family and friends for forever encouraging me to push myself to new levels. To those I was not able to mention by name, I thank you always for your support and encouragement.

This work was support by funding from U.S. Department of Defense, Defense Threat Reduction Agency (DTRA) grants, HDTRA1-17-1-0026 and HDTRA1-16-1-0020.

Contents

LIST OF FIGURES

LIST OF TABLES

CHAPTER 1: INTRODUCTION TO SPECTROSCOPY AND METHODOLOGY

1.1 Motivation

Spectroscopy is a technique for experimentally determining the characteristic electromagnetic spectrum that results from changes in energy of the material. These changes in energy are due to electronic, rotational, vibrational, and translational transitions that release a discrete amount of energy that corresponds to a photon of a specific wavelength [1]. Many techniques have been developed for measuring these signatures. The utility of the technique is that it can be used to remotely characterize a phenomenon without disrupting it.

One such application of this technique is nuclear forensics and remote sensing. Of interest is detecting signatures of actinide species and oxides in particular, which are a largely radioactive group of elements that could potentially be used for the development of nuclear devices. It is of importance to understand the spectral signatures that these species produce so that they can be detected as well as be able to detect and analyze the products of fallout after a nuclear detonation. These results could be used to better inform those in the affected area, military personnel, and disaster-relief responders of the dispersal of species and radioactivity after such an event as well as help develop tools to model fallout formation.

Understandably, it is not practical to perform this kind of testing on a ‘real-life’ scale at any frequency due to effects on surroundings, the difficulty in procuring some actinide materials, and other factors. Thus analogous testing is necessary to acquire the spectral information necessary. Work is being done to characterize the spectral signatures of actinides in the near ultraviolet (UV) and visible (VIS) ranges via various excitation methods, such as sparking, explosive detonation, laser discharge, and flame under different conditions. The resulting signatures can be used to develop an understanding of how species react and interact during and following a detonation. Various approaches are being taken to develop a base of information about these actinide materials. Some entities are working on models to simulate the reaction mechanisms of various actinides and fallout formation calibrated by small-scale laboratory testing, while others are experimentally observing these signatures in larger-scale testing [2]–[4]. This work deals primarily with small-scale testing to identify and track changes in these signatures.

1.2 Theory

1.2.1 Spectroscopy

On a basic level, transitions between energy levels can lead to the emission or absorption of photons. Figure 1 depicts the three types of atomic electronic transitions between two states: these include spontaneous emission, quantified by the Einstein A coefficient (A_{21}), stimulated emission (B_{21}), and absorption (B_{12}) [5].

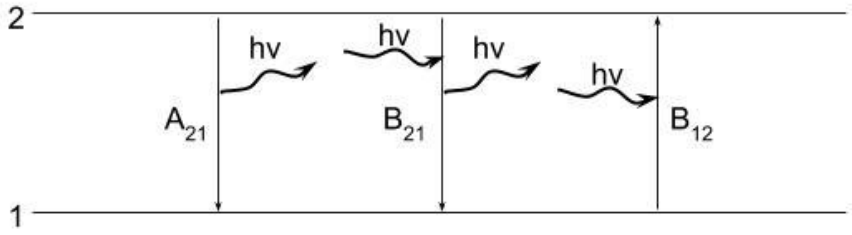

Figure 1: Atomic emission and absorption transitions.

Photon energy is denoted by E, where h is Planck's constant (6.626E-34 m^2kg/s), ν is the frequency of the transition, λ is the wavelength, and c is the speed of light (Equation 1). More complex transitions also emit and absorb light.

$$E = h\upsilon = \frac{hc}{\lambda} \qquad \textit{Equation 1}$$

Emission and absorption can occur across the electromagnetic spectrum which can range from gamma rays (high energy, short wavelength) to radio waves (low energy, high wavelength). Electronic transitions largely occur in the UV and visible ranges of the spectrum. When a material is excited, many electrons can change energy states and emit photons of various energies/wavelengths. These varying transitions will occur in different proportions, creating a spectrum of peaks that occur at varying intensities. A higher intensity at a certain wavelength corresponds to more electrons going through that transition. These intensities can change with the temperature of the species studied, and thus spectroscopy has great utility in experimentally and non-invasively determining temperature. An example of this change in spectrum with temperature is shown in Figure 2.

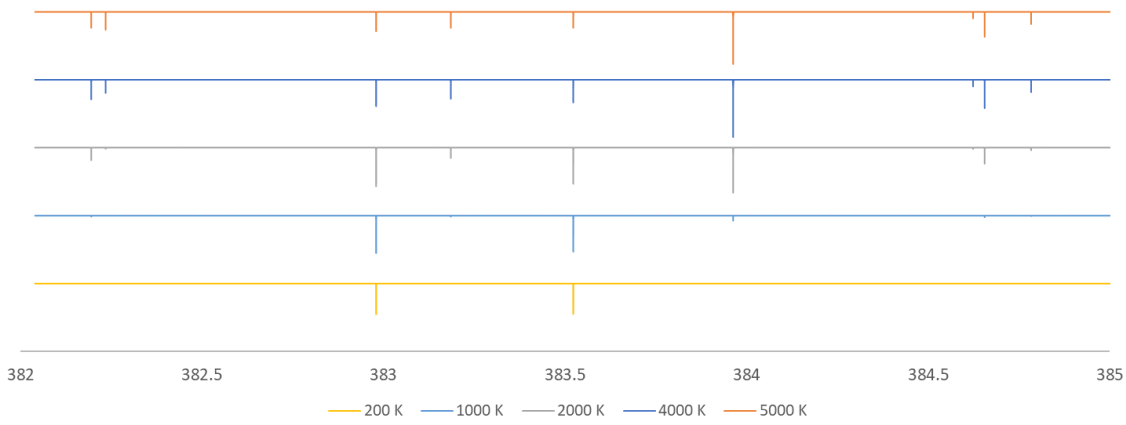

Figure 2: Simulated change in U I spectrum with temperature in 382-385 nm range.

As temperatures increase, more transitions appear and ratios between intensities change (energy levels are populated in different proportions). If additional information about the species and experimental setup are known and a spectral line profile can be determined, a concentration can be calculated as well. This process of determining temperature and concentration from an absorption spectrum is outlined in Sections 1.2.3 and 1.2.4.

1.2.2 Instrumentation

These characteristic spectra can be observed utilizing devices called spectrometers. There are several types of spectrometers, but this work refers to the optical spectrometer specifically. Light entering a spectrometer is diffracted into orders and is either passed through (transmission grating) or reflected (reflective grating) [6]. Figure 3 is a simplified depiction of how a spectrometer operates.

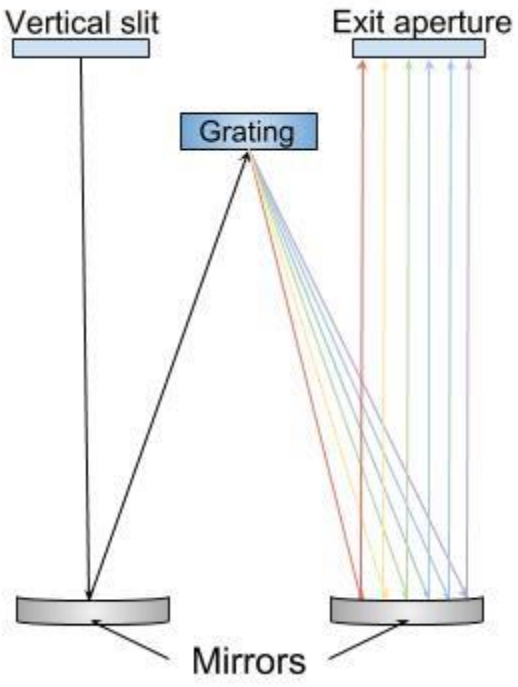

Figure 3: Simple spectrometer diagram with reflective grating.

The angle of the grating can be altered to change the region of the electromagnetic spectrum that is observed at the exit of a given spectrometer. Groove density of the grating and the dimensions of a spectrometer can also be altered to target differently-sized ranges. Various regions of the electromagnetic spectrum are challenging to observe and require additional experimental consideration. As an example, the vacuum ultraviolet (100-200 nm) requires that the light path from the event through the spectrometer be in vacuum or be purged with nitrogen or argon to avoid absorption by the oxygen in air. Light is collected at the output of a spectrometer utilizing a detector, such as a charge-coupled device. Once the light is collected, it can be processed into a spectrum, from which temperature and concentration of various species can be obtained.

1.2.3 Atomic Electronic Temperature and Concentration Calculation

To calculate the temperature of an electronic transition, certain information is required about each of the states involved. Equation 2 shows the calculation of a Boltzmann temperature which requires knowledge of the energy levels, state degeneracies, and populations at each state, as well as the Boltzmann constant of 1.38E-23 $m^2kg/(s^2K)$.

$$T_{el} = \frac{\varepsilon_k - \varepsilon_j}{k_B ln(\frac{g_k n_j}{g_j n_k})}$$ *Equation 2*

To determine the populations at each state for electronic absorption, Equation 3 can be employed. W_{lu} is the integrated absorption, which is the area under the transition peak in absorption. Note that this is under the assumption that the medium is optically thin.

$$n_l = \frac{cW_{lu}}{h\upsilon_{ul}B_{lu}L}$$ *Equation 3*

Degeneracy, which is the number of possible states for a given level, and the energy at a given level are known values. Once these values are determined, one more quantity is still required to calculate the total concentration of a material. Z_{el} is the electronic partition function, which can be calculated as outlined in Equation 4.

$$Z_{el} = g_0 + \sum_i g_i e^{-\frac{\varepsilon_i}{k_B T}}$$ *Equation 4*

Consequently, concentration, n, can then be calculated (Equation 5).

$$\frac{n_i}{n} = \frac{g_i e^{-\frac{h\nu}{k_B T}}}{Z_{el}}$$ *Equation 5*

1.2.4 Molecular Temperature

For SiO, information necessary to model the $A^1\Pi$-$X^1\Sigma^+$ (1,0) band were obtained from Hermann et al. and the NIST diatomic molecule database [7], [8]. To obtain temperatures, experimental data was overlaid with the model in PGOPHER, a program utilized for simulating spectra, to find the temperature at which the shapes of the experimental and modeled data were the same [9].

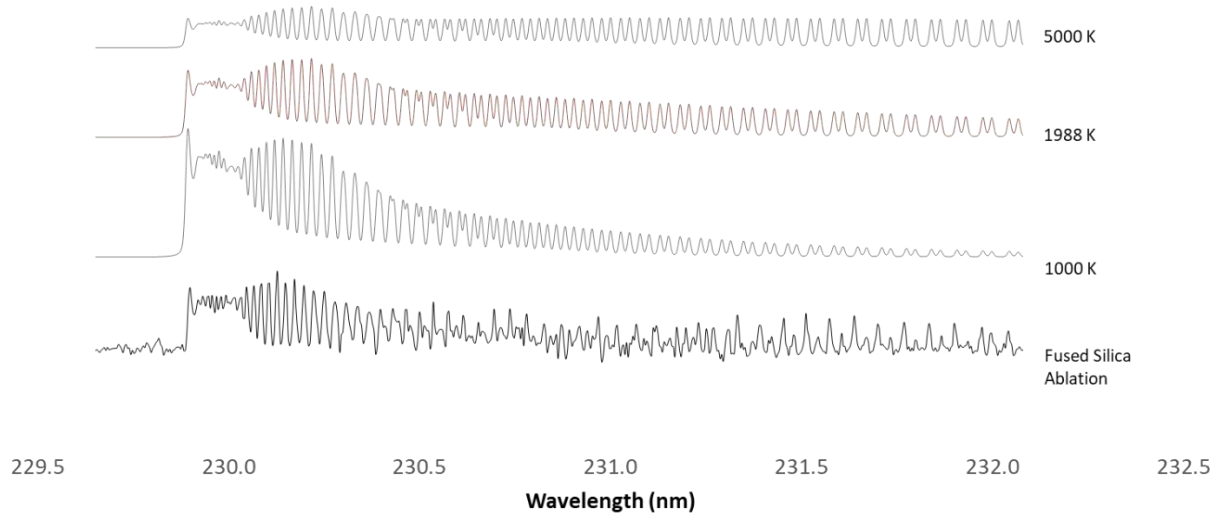

Figure 4: SiO $A^1\Pi$-$X^1\Sigma^+$ transition (1,0) band overlaid with absorption signature from ablated fused silica sample for calculation reference. This SiO molecular temperature of ablated fused silica appears to be about 1988 K. Models of the band at various temperatures are shown to highlight the change in band structure with temperature.

1.2.5 Optical Thickness Correction

Curve of growth calculations were employed to correct for optical thickness in the temperature and concentration calculations. It was determined in Glumac et al. that optical depth corrections were significant in early time spark measurements for LIBS, and were therefore applied [10]. To determine the curve of growth, the Voigt profile must be calculated. The Voigt profile is the convolution of a Gaussian profile and a Lorentzian profile, which manifest from Doppler line broadening due to temperature effects, and collisional line broadening due to pressure effects, respectively. Due to the complexity in calculation of a true Voigt profile, an approximation (the pseudo-Voigt profile) is used instead (Equation 6)[11].

$$f_{pV}(x) = (1-\eta)f_G + \eta f_L \qquad \textit{Equation 6}$$

Here f_G refers to the Gaussian profile from Doppler broadening, f_L refers to the Lorentzian profile from collisional broadening, and η is a non-dimensional parameter. Shown in Equation 7 is the calculation of the pseudo-Voigt full width at half maximum (FWHM) from the Doppler and collisional FWHMs (Equation 8 and Equation 9) [1], [11].

$$w_{pV} = (w_D^5 + 2.69269w_D^4w_C + 2.42843w_D^3w_C^2 + 4.47163w_D^2w_C^3 + 0.07842w_Dw_C^4 + w_C^5)^{1/5} \quad \textit{Equation 7}$$

$$Doppler\ FWHM = w_D = \lambda_0\sqrt{\frac{8kTln2}{mc^2}} \quad \textit{Equation 8}$$

$$Collisional\ FWHM = w_C = \frac{2Z^*}{\pi} \quad \textit{Equation 9}$$

Where Z^* is the collisional frequency:

$$Z^* = \frac{\pi pkT\sigma^2}{\sqrt{2}}\sqrt{\frac{8kT}{\pi m}} \quad \textit{Equation 10}$$

Here, p is pressure, k is the Boltzmann constant, T is temperature, σ is collisional cross section, and m is mass. Once Doppler width and collisional width are obtained, η can be calculated and applied to calculate the pseudo-Voigt profile (Equation 11) [11].

$$\eta = 1.36603\left(\frac{w_C}{w_D}\right) - 0.47719\left(\frac{w_C}{w_D}\right)^2 + 0.11116\left(\frac{w_C}{w_D}\right)^3 \quad \textit{Equation 11}$$

An iterative process is then used to calculate the equivalent width and integrate the pseudo-Voigt curve for a series of optical depth guesses to obtain a more correct optical depth and linear equivalent width. Temperature is recalculated using the newly-obtained equivalent widths and reapplied to the concentration calculations for an adjusted result.

1.3 Methodology

1.3.1 Laser Induced Breakdown Spectroscopy

Laser Induced Breakdown Spectroscopy (LIBS) involves the focusing of a laser beam onto a target material, producing a plasma that can be optically characterized. Due to plasmas having high temperatures and pressures, the spectral signal is strong in emission and ionization can be observed [1]. It is relatively non-destructive to the material and requires little in the way of sample preparation. LIBS has the capacity for high speed, time-resolved, and *in situ* measurements, and can be used to detect neutral and ion spectral features for both atomic and molecular species [12]. It has been used in a wide variety of applications since its inception in the 1980s, including environmental analysis, combustion system analysis, quality control of pharmaceutical products, and biomedical applications among others [12], [13].

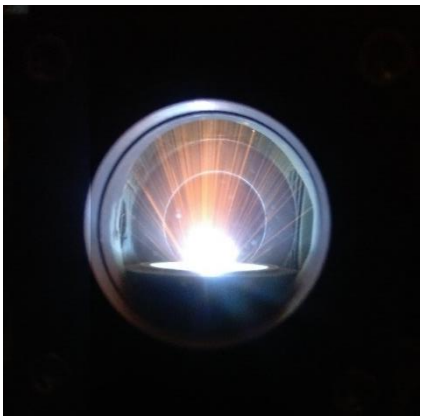

Figure 5: Laser induced plasma emission from a uranium wafer.

1.3.2 Absorption Spectroscopy

Absorption spectroscopy involves measuring the absorption of energy at various frequencies by a material when subjected to a broadband source of radiation. When the source of radiation, whether flash lamp, LED, etc. is shone through a sample, light will be transmitted sans that which was absorbed by the material at characteristic frequencies/wavelengths. The degree to which this absorption occurs can be quantified and used to evaluate such parameters as temperature and concentration of a species and consequently is invaluable as a method of characterization. Absorption spectroscopy can be used in conjunction with a variety of other experimental methods including LIBS. It is important to note that this technique is limited by the path length, the line-of-sight along which absorption is measured. Any information obtained such as temperature and concentration reflect all absorption occurring along this path, which means that any variations along that path cannot truly be resolved. Concentration is averaged along the path and temperature is convolved.

1.4 Previous Work

Laser induced breakdown spectroscopy is a long-established method. It has been used extensively to characterize metal plasmas in varying environmental conditions. Glumac et al. observed temporal evolution of emission intensity of a laser spark in air from delays of 50 ns to around 2 μs. The size of the spark was tracked as well as variations in intensity throughout a given event [10]. Ma et al. spatially characterized a laser-induced plasma on an aluminum target. They were able to obtain emission spectra at various time delays and calculate temperature and number density parameters accordingly as a function of axial and radial distance and time [14]. A kinetic

model of a metallic Pb LIBS plume was used by Babushok et al. to simulate an environment with varying O_2 content to determine trends in population. This model was calibrated with information derived from experimentally-obtained emission spectra [15]. Gleason et al. studied the effect of oxygen on detection of mercury atomic emission of a laser-induced plasma [16].

Particularly relevant to this research is the characterization of Uranium plasma. Skrodzki et al. looked at the evolution of various U lines in a microsecond time scale in both atmospheric and 100 torr air and nitrogen environments, as well as the persistence of the uranium plasma signal over time at various pressures [17]. Zhang et al. studied uranium plasma spectra in air, argon, neon, nitrogen, and oxygen in the visible and near-UV regions [18]. Harilal et al. studied the spatial dependence of spectral signal on pressure over time in air and persistence in air and argon for different pressures [19]. Additionally, Harilal et al. characterized UO molecular emission in varying pressure conditions [20]. Miyabe et al. investigated the temporal evolution of a uranium ablation plume in vacuum and helium environments using absorption LIBS to determine the flow velocity of the plume front [21]. Zhang et al. observed variation in emission signal intensity of U I and U II when ambient gas and flowrate were altered [18].

These experimental measurements are needed to more comprehensively catalog spectral signatures under different conditions and calibrate theoretical models that are currently being developed to model kinetics of the laser induced uranium plasma [3]. These models will eventually be used to analyze nuclear debris and fractionation processes in actinides in conjunction with the spectral data gathered. CRAFT Tech is also working to model early-time nuclear post-detonation fireball phenomena [4].

1.5 Scope

This document details work using LIBS to characterize species present in nuclear fallout in order inform fireball model development. Multiple species were identified and tracked temporally, including U I, U II, UO, Si I and SiO. The UO molecular band was tracked temporally and over varying environmental conditions. U I and U II species were tracked over time and in different concentrations of environmental O_2. This work will present the experimental and post-processing methodology as well as summarize trends in fireball temperature and concentration.

CHAPTER 2: SPECIES OF INTEREST

2.1 LIBS Plasma Behavior

The laser-induced plasma is dynamic and can vary greatly with changes in ambient pressure and composition of gaseous environment regardless of the base material. Currently, models are in development by researchers at the University of Illinois and CRAFT Tech to simulate oxidation and development of U_xO_y species in a laser-ablated uranium plume [3], [4]. While these models require calibration from physical experiments, they also draw from the kinetics of other more well-studied species and general trends in plasma behavior. Much work has been performed at various laser power inputs, pulse schemes, and so on.

When the incoming laser beam strikes the surface of a sample, energy is deposited into the material, and a vapor is formed. This vapor becomes a plume of the material as it begins to emit light and dissipates (Figure 6) [22]. The material can then combine with elements from ambient gas to form related molecules such as oxides of the material in question. These oxides do not necessarily form homogeneously.

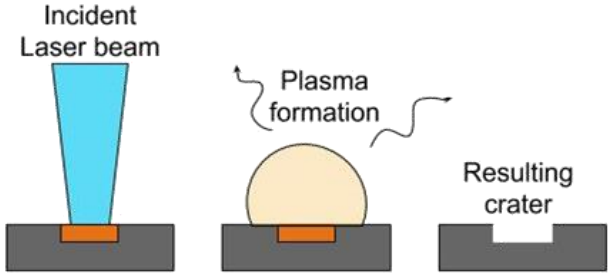

Figure 6: Simplified laser-induced plasma formation diagram.

Plasma duration can change greatly depending on the surrounding environment and is typically on the microsecond scale. The spectral readout can vary greatly depending on the aforementioned conditions. It also changes spatially depending on which part of the plasma is being probed, as the constituents are not necessarily equally dispersed throughout the plasma and temporally if the plasma is being generated by a pulsed laser and not a continuous source. Although dynamic, a pulsed laser-induced plasma is relatively repeatable, which allows for reliable characterization.

2.2 Uranium Oxidation Mechanism

Finko et al. developed a model for early formation of uranium molecular oxides in laser-induced plasma based on Al_xO_y metal-oxygen system [3]. They found that electron and ion formation occur at much earlier times than higher oxides. This work was referenced for both detecting the relevant species and the timescales at which they form with respect to one another. For the purposes of this document, U I, U II, and UO were tracked; later attempts will be made to characterize other U_xO_y species, such as UO_2 and UO_3 which form at later times. Many scientists have successfully observed the formation of uranium oxides under various conditions in emission [17], [23]–[25]. These works were drawn from to determine conditions that might be conducive to the observation of uranium species in absorption.

2.3 Silicon and Oxide Species

The presence of other species can affect and be affected by the breakdown of uranium species in a fireball. Silicon is one of the most abundant materials and therefore is very likely to play a part in the fractionation of post-nuclear detonation products. The presence of silicon could affect the uranium reaction mechanism by displacing other constituents or by causing a redistribution of energy available. This information is vital for the analysis of nuclear debris, as it will better represent actual conditions [2]. For this reason, a sample containing both uranium and silicon was ablated. Species pertaining to both were observed for comparison of temperature and concentration trends where possible. Future work will be done in characterizing fractionation in the presence of other commonly occurring species, such as iron.

2.4 Targeted Transitions

This section serves to summarize the transitions observed in order to determine temperature and concentration of the species tracked as well as demonstrate that these transitions are suitable yield valid data in the appropriate temperature range.

There are many U I and U II transitions located in the near ultraviolet region of the electromagnetic spectrum. Several of them are especially strong due to their lower energy levels occurring at the ground state. Figure 7 shows labeled transitions used for U I and U II atomic temperature calculations in this region. The information necessary for these calculations obtained from the Kurucz Atomic Spectral Line Database is listed in Table 1 and Table 2 [26].

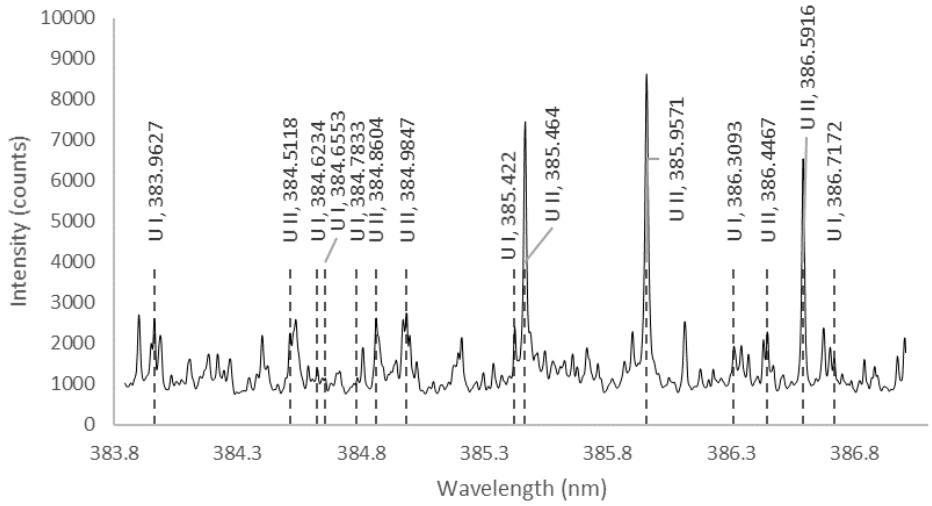

Figure 7: Emission spectrum with U I and U II transitions used for temperature calculation obtained from Kurucz Database [26].

Figure 8 and Figure 9 are Boltzmann fraction plots for U I and U II in the near ultraviolet region to show sensitivity of the various transitions to temperature. The Boltzmann fraction is a permutation of Equation 2 which represents the fraction of atoms or molecules in a certain energy state. In this case, Boltzmann fraction is shown varied with temperature.

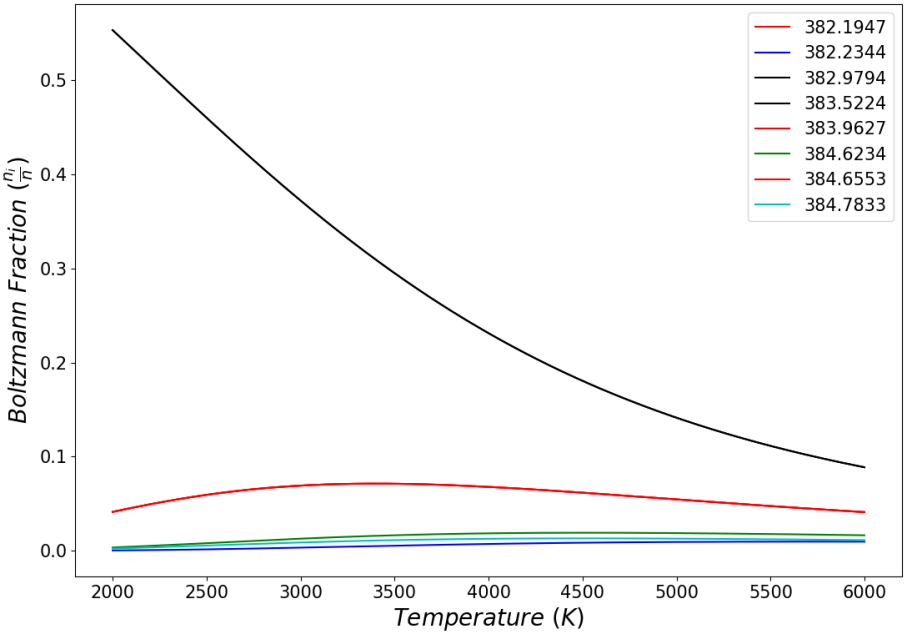

Figure 8: Boltzmann Fraction vs. Temperature for U I lines used for calculation in 382-385 nm range.

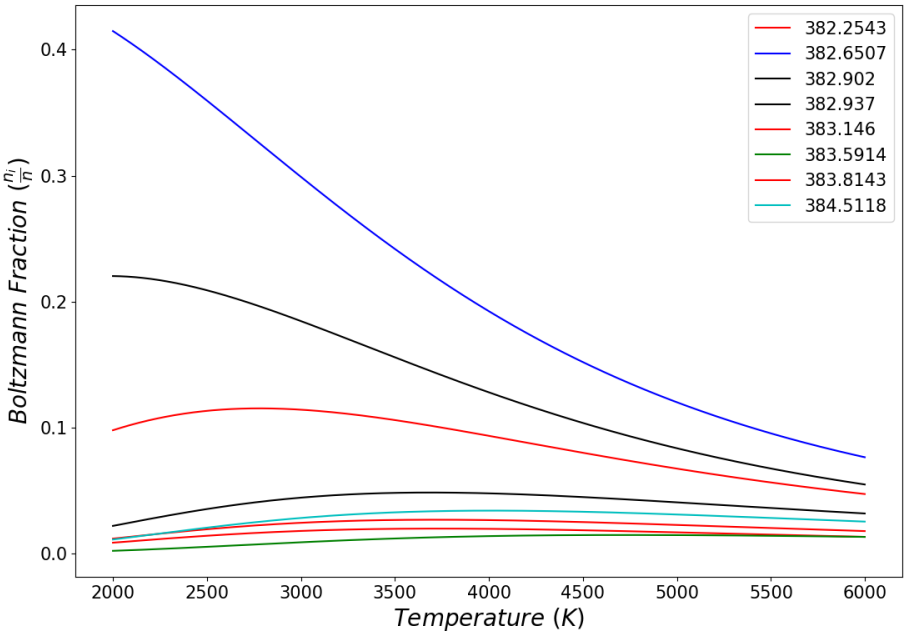

Figure 9: Boltzmann Fraction vs. Temperature for U II lines used for calculation in 382-385 nm range.

For some transitions and in some temperature ranges, this fraction remains somewhat constant with temperature, indicating that the particular transition is not sensitive to temperature in the desired range. However, the opposite also holds. For example, in Figure 9 the transition corresponding to 382.6507 nm shows strong dependence on temperature. Whereas the transition at 384.5118 nm shows relatively weak dependence on temperature. When all transitions are considered, using Equation 2, a reasonably accurate temperature for a given species can be determined.

The 593.55 nm UO band is one of the more commonly-studied UO bands. The region observed also features several U I transitions which were used to calculate atomic temperature and concentration (Figure 10, Table 1).

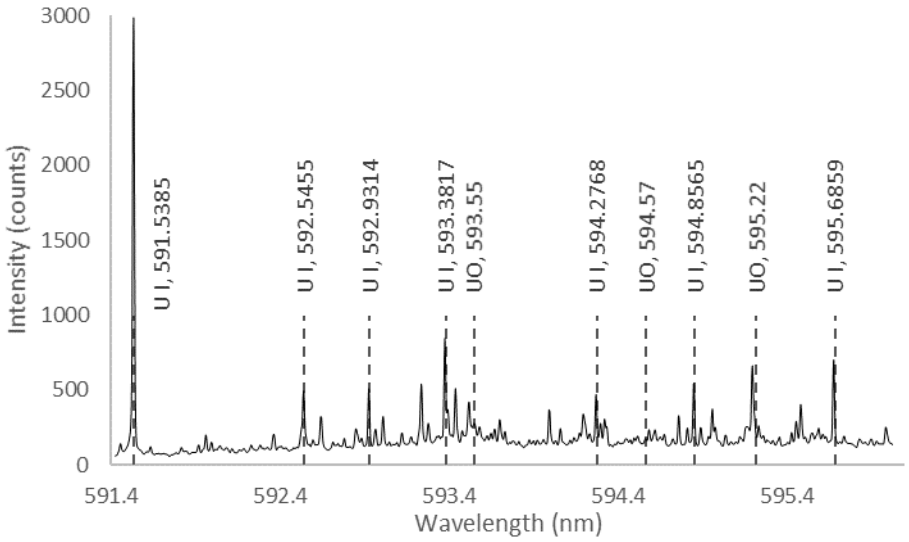

Figure 10: Emission Spectrum in Region around 591-596 nm. Labeled U I lines from Kurucz Database were used for temperature calculation. Labeled UO lines are from work done by Mao et al [26][24].

Table 1 details all tabulated information used for U I temperature and concentration calculations [26]. Figure 11 shows the Boltzmann fraction versus temperature plot for U I transitions in this region.

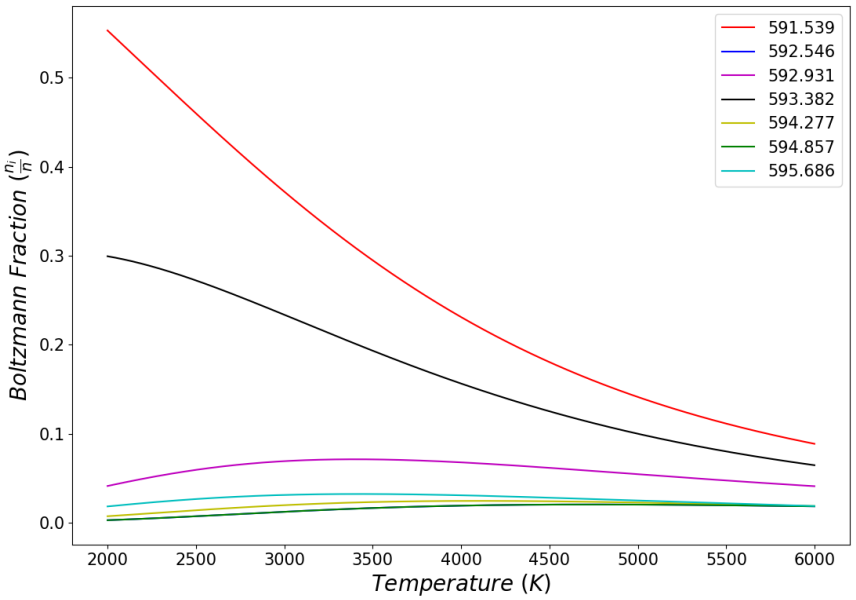

Figure 11: Boltzmann Fraction vs. Temperature for U I lines used for calculation in 591-596 nm range.

Table 1: Wavelengths, Einstein Coefficients, energy levels, and J terms of selected transitions for U I [26].

Species	λ (nm)	A_{ul}	B_{lu}	B_{ul}	E_{lower} (cm^{-1})	J_l
U I	382.195	2.55E+07	8.56E+19	8.56E+19	3800.83	7
U I	382.234	8.09E+07	2.39E+20	2.71E+20	10347.3	8
U I	382.979	4.98E+06	1.68E+19	1.68E+19	0	6
U I	383.522	5.83E+06	1.67E+19	1.98E+19	0	6
U I	383.963	1.24E+08	4.21E+20	4.21E+20	3800.83	7
U I	384.623	3.50E+07	1.20E+20	1.20E+20	7005.53	6
U I	384.655	2.45E+07	8.38E+19	8.38E+19	3800.83	7
U I	384.783	1.09E+08	2.89E+20	3.71E+20	7020.71	4
U I	385.422	2.47E+07	8.49E+19	8.49E+19	0	6
U I	386.309	2.61E+07	9.04E+19	9.04E+19	3868.49	3
U I	386.717	1.26E+08	3.40E+20	4.38E+20	7020.71	4
U I	591.539	9.52E+05	1.37E+19	1.18E+19	0	6
U I	592.546	6.45E+05	9.01E+18	8.06E+18	7645.65	8
U I	592.931	2.90E+05	3.15E+18	3.63E+18	3800.83	7
U I	593.382	1.30E+05	1.33E+18	1.63E+18	620.323	5
U I	594.277	3.45E+05	3.56E+18	4.35E+18	5762.08	5
U I	594.857	4.33E+05	5.47E+18	5.47E+18	7645.65	8
U I	595.686	7.57E+05	6.86E+18	9.61E+18	3868.49	3

Table 2 details U II tabulated spectral information.

Table 2: Wavelengths, Einstein Coefficients, energy levels, and J terms of selected transitions for U II [26].

Species	λ (nm)	A_{ul}	B_{lu}	B_{ul}	E_{lower} (cm^{-1})	J_l
U II	382.254	3.98E+06	1.78E+19	1.33E+19	4706.28	2.5
U II	382.651	4.06E+06	1.59E+19	1.36E+19	289.036	5.5
U II	382.902	2.16E+06	7.28E+18	7.28E+18	914.758	4.5
U II	382.937	4.01E+06	1.16E+19	1.35E+19	4585.43	6.5
U II	383.146	5.17E+07	2.18E+20	1.75E+20	4663.8	3.5
U II	383.591	9.77E+06	3.31E+19	3.31E+19	7598.36	5.5
U II	383.814	2.62E+06	7.41E+18	8.90E+18	2294.69	5.5
U II	384.512	3.22E+06	9.42E+18	1.10E+19	5526.75	6.5
U II	384.86	9.10E+06	3.11E+19	3.11E+19	5259.65	7.5
U II	384.985	1.68E+06	4.61E+18	5.76E+18	0	4.5
U II	385.464	5.97E+07	2.57E+20	2.05E+20	4663.8	3.5
U II	385.957	2.51E+07	1.01E+20	8.67E+19	289.036	5.5
U II	386.447	5.87E+06	2.54E+19	2.03E+19	4663.8	3.5
U II	386.592	1.98E+07	6.87E+19	6.87E+19	2294.69	5.5

Table 3 lists the information relevant to calculation of Si I temperatures, a potential species observed in fractionation of post-detonation products.

Table 3: Wavelengths, Einstein Coefficients, energy levels, and J terms of selected transitions for Si I [26].

Species	λ (nm)	A_{ul}	B_{lu}	B_{ul}	E_{lower} (cm-1)	J_l
Si I	298.7645	2.66E+06	2.56E+18	4.25E+18	6298.85	2
Si I	300.6739	1.10E+03	2.99E+15	1.80E+15	77.115	1
Si I	302.0004	3.30E+03	5.46E+15	5.46E+15	223.157	2

The corresponding Boltzmann fraction follows (Figure 12).

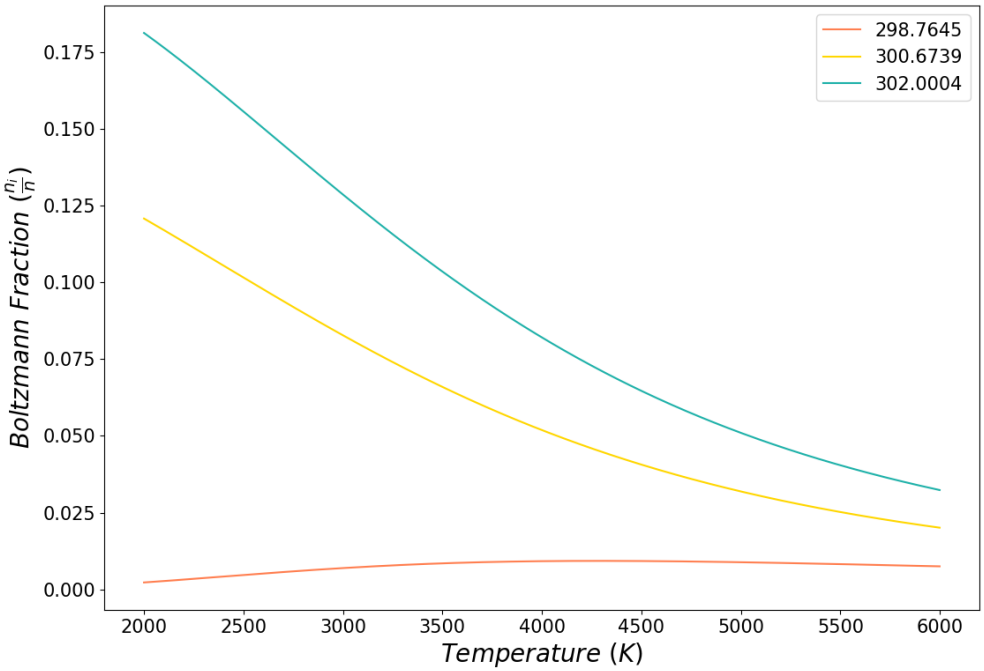

Figure 12: Boltzmann Fraction vs. Temperature for Si I lines used for calculation in 298-303 nm range.

Figure 13 shows a transmission spectrum of the SiO $A^1\Pi$-$X^1\Sigma^+$ transition in the ultraviolet that was additionally pinpointed in this study. This transition provided rotationally-resolved peaks that allowed for molecular temperature fitting with the PGOPHER program as discussed in 1.2.4.

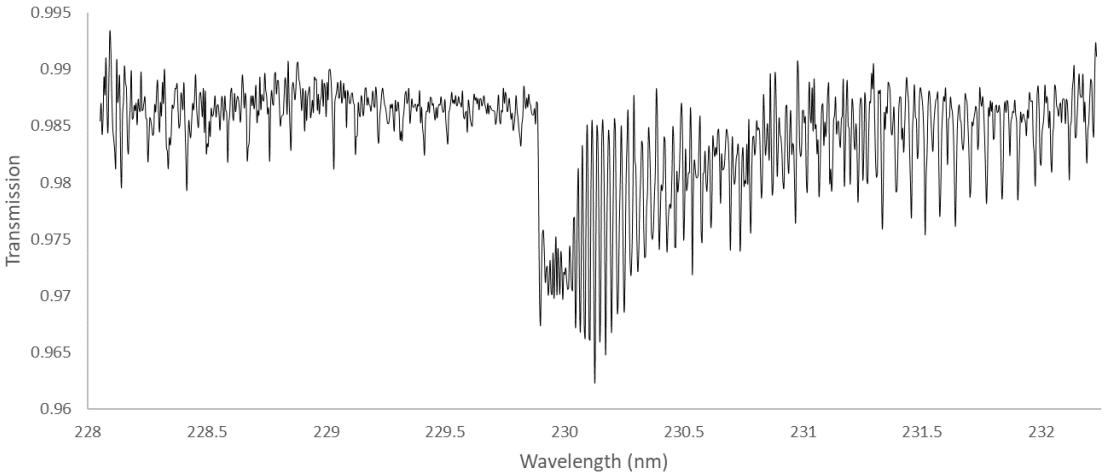

Figure 13: Transmission spectrum of SiO $A^1\Pi$-$X^1\Sigma^+$ (1,0) Band at 230 nm.

CHAPTER 3: EXPERIMENTAL SETUP

3.1 Safety Equipment

Appropriate safety protocol was followed as outlined by the Division of Research Safety at the UIUC. Whenever uranium was handled, full-face respirators with HEPA filters were used to eliminate the possibility of heavy metal inhalation. Materials used to clean any chamber in which uranium testing was performed were stored and disposed of as per regulation. Uranium samples were always stored in sealed environments, which were appropriately labeled [27].

Laser glasses were used by all present when the Nd:YAG laser was in operation. A red warning lamp outside of the room was turned on whenever the laser was on to warn those who might otherwise enter the room of the potential hazard. Compressible gases were also used frequently over the course of this research for controlling the test environment, and the appropriate precautions were taken [28].

3.2 Absorption Laser Induced Breakdown Spectroscopy Setup

One of the advantages of laser induced breakdown spectroscopy is that it requires relatively little sample preparation. Flat samples of U_{238} were ablated on a rotating stage to avoid drilling into the sample (Figure 14, Figure 16). The U_{238} sample was used for all tests involving environmental variation, and a U_3Si_2 sample created at Lawrence Livermore National Laboratory was used for the tests capturing U I, U II, Si I, SiO, and UO signatures temporally. The U_3Si_2 sample was created by arc melting depleted uranium and elemental silicon.

Figure 14: Uranium wafer sample (left), U_3Si_2 sample (right).

The sample was contained in a chamber was kept under vacuum and various gases were seeded in continuously to a given pressure (Figure 15(a), Figure 18).

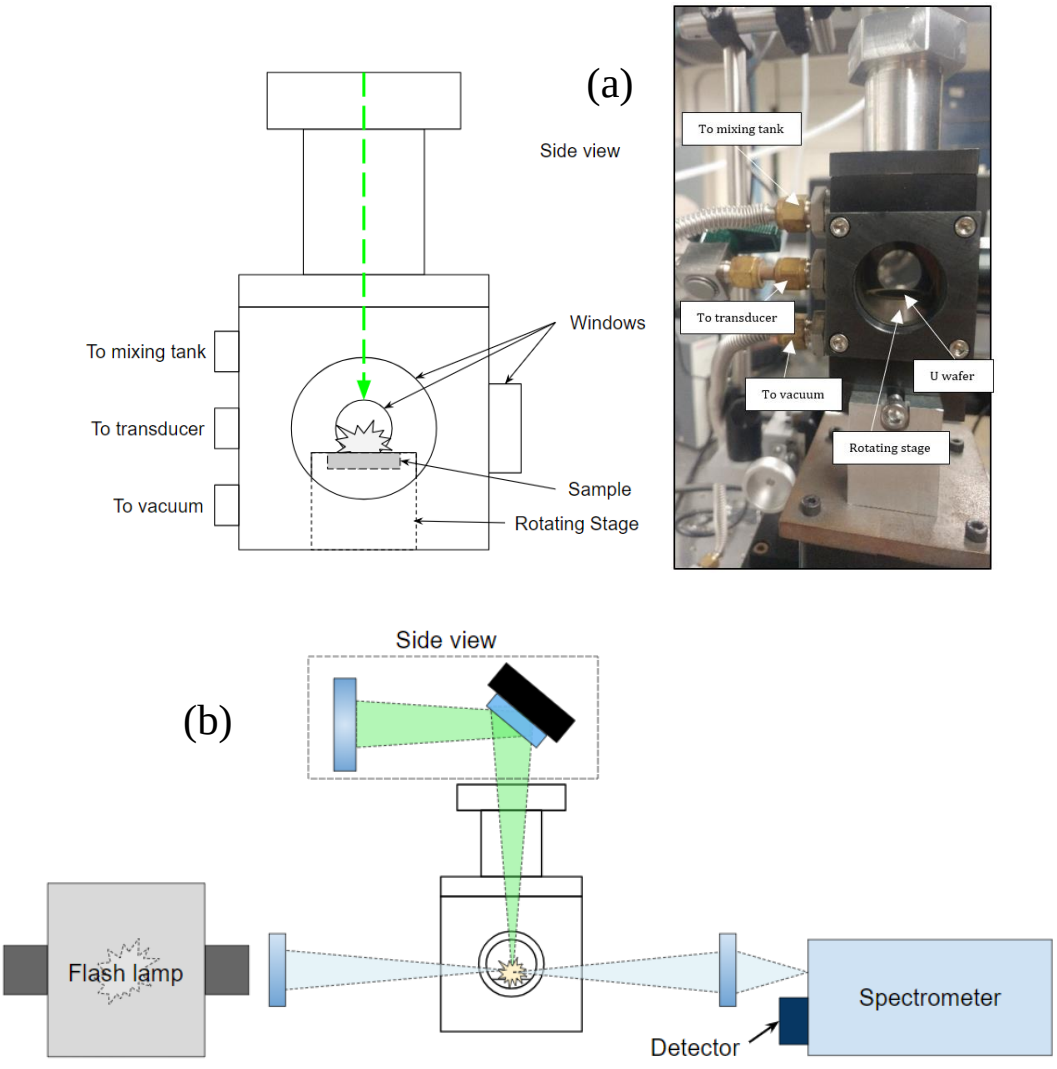

Figure 15: Schematic of LIBS chamber (a) and absorption setup (b). The Nd:YAG pulse is directed to and focused at the sample from above the chamber using a series of optics.

A frequency-tripled Nd:YAG laser (Spectra-physics, model no.: PS-100) set to 85 mJ output was focused at the surface of a sample from the top of the chamber using a series of optics (Figure 17). A flash lamp (Oriel Instruments 6427) was positioned in line with the chamber and spectrometer (Figure 15(b)). The flash lamp (Oriel Instruments 6427) was triggered with a pulse generator (Quantum Composers 9514) signal to its power supply (Oriel Instruments 68826) (Figure 19). The pulse generator in turn was triggered by the Nd:YAG laser module. To take images at various

'delay times' the flash lamp output was varied with respect to the Nd:YAG pulse by changing the amount of time between the pulse generator accepting a trigger signal from the Nd:YAG and sending a trigger signal to the flash lamp (Figure 19). The entire absorption LIBS setup is shown in Figure 20.

Figure 16: Rotating stage motor and Electro Industries power supply.

Figure 17: Spectra-Physics Nd:YAG Laser (top) and Control Panel (bottom).

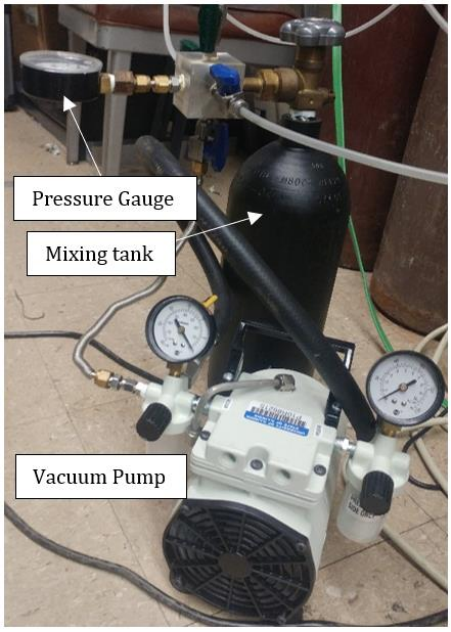

Figure 18: Gas mixing setup.

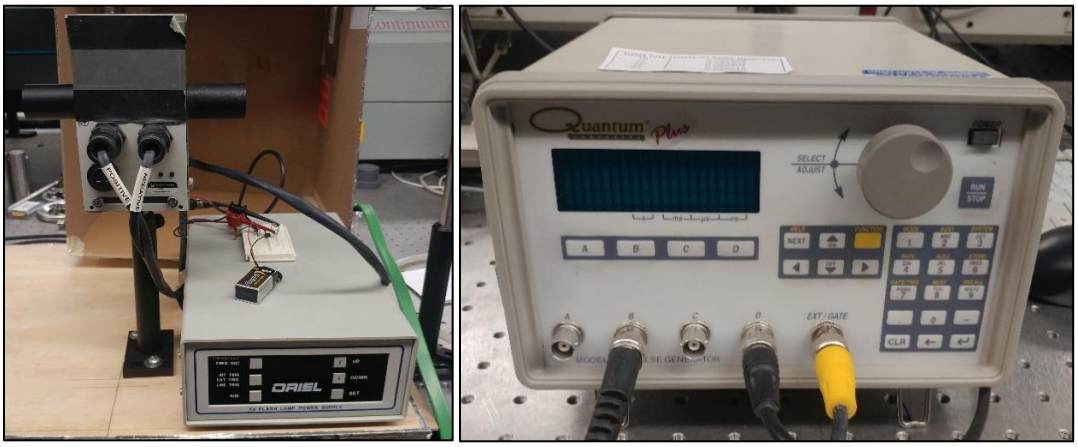

Figure 19: Oriel Instruments Flash lamp (left) & Quantum Composers pulse generator (right).

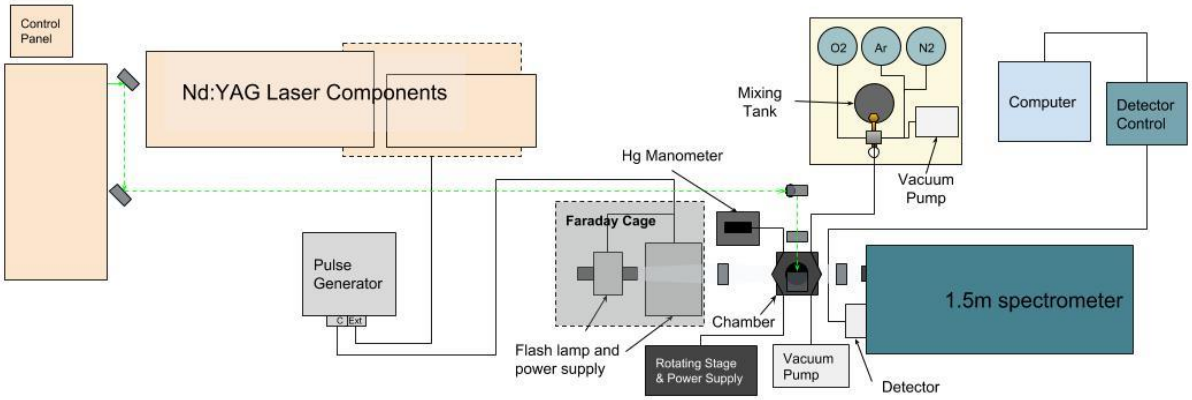

Figure 20: Full Absorption LIBS setup.

3.3 Data Acquisition Scheme and Processing

Measurements were taken using an Andor iDus 420 charge-coupled device (CCD) or a Hamamatsu C7557-01 multichannel detector and a 1.5-meter dispersive spectrometer at the various visible ranges necessary to target the species studied (employing 2400 gr/mm and 3600 gr/mm gratings as necessary) (Figure 21 and Figure 22). These ranges were discussed in Section 2.4. The timing at which the flash occurred was delayed with respect to the onset of the pulse so that development of the LIBS plasma could be observed at different points in time.

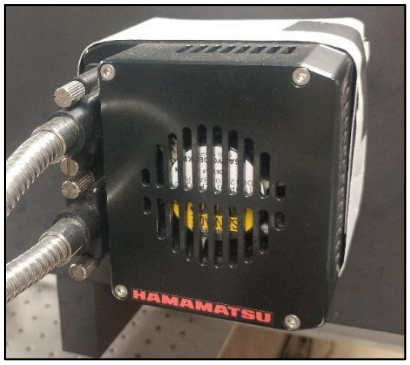

Figure 21: Hamamatsu C7557-01 Multichannel Detector.

Figure 22: Andor iDus charge-coupled device.

Figure 23 shows a graphical explanation of the transmission data acquisition. Prior to ablation, a file with alternating frames of 'dark' and flash lamp spectra was taken. During ablation, a binned spectral intensity file with alternating frames with emission and absorption occurring was captured. For a single test, 50 of each type of spectrum was taken and processed into a single averaged transmission spectrum. Figure 23 shows the timing of the flash lamp, Nd:YAG pulse initially ablating the sample, and detector acquisition with relation to each other as well as sample output spectra used to obtain a transmission spectrum. The figure shows the acquisition window for the Andor CCD. When the Hamamatsu detector was used, it had a slightly longer window of acquisition time, but was otherwise triggered with the same timing scheme. The advantage of the Andor CCD over the Hamamatsu detector was higher sensitivity, although both detectors in combination with the spectrometer provided the ability to obtain high-resolution spectra conducive to quantitative measurement and calculation of parameters such as temperature and number density of species.

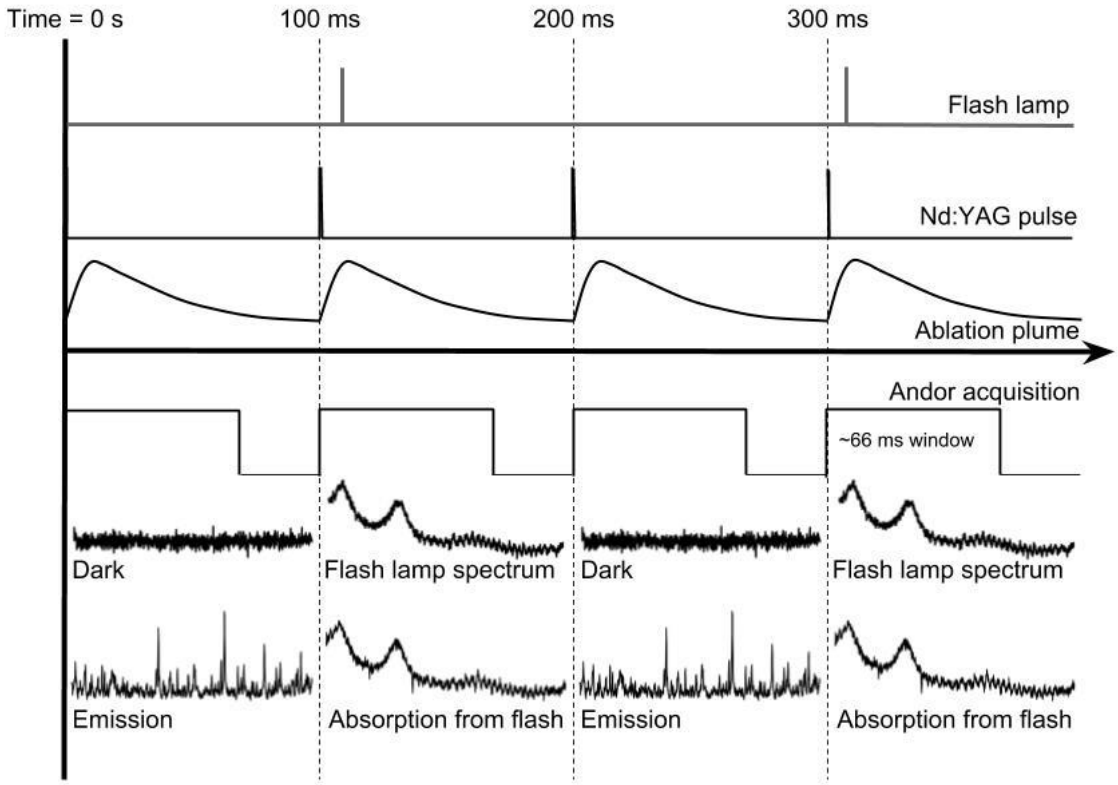

Figure 23: Timing scheme for transmission data acquisition. The flash lamp pulses, Nd:YAG pulses, and luminescence from ablation plume (when Nd:YAG pulse is not blocked) are shown above the axis; CCD frame acquisition, and sample test data are shown below the axis. (a) acquisitions with blocked laser pulse for dark and flash lamp reference spectra (b) acquisitions with laser pulse ablating sample.

Data was processed using a series of codes produced in Python [29]. Figure 24 shows an example of a transmission spectrum after processing raw input data similar to that seen at the bottom of Figure 23. In essence, light produced from the background, flash lamp, and emission are divided and subtracted out using the relation described in Equation 12, leaving only transmission.

$$Transmission = \frac{(Source + Plume) - Plume\ Emission}{Source - Dark} \qquad \textit{Equation 12}$$

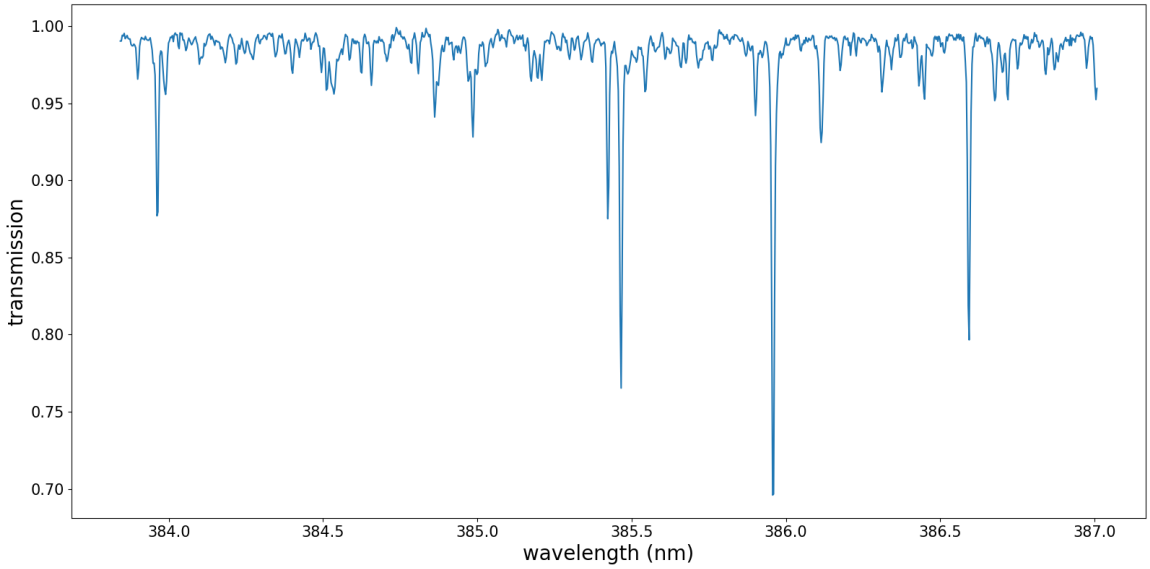

Figure 24: Example Processed Spectrum (15 torr ambient pressure, 2% O2/98% Ar gas fill, 5 µs delay time).

A code in python converted transmission spectra to absorption spectra and found the areas under the peaks chosen for temperature and concentration calculation. The calculations were performed as outlined in Section 1.2.3 and took into account the optical depth corrections outline in Section 1.2.5. The test shown in Figure 24 yielded a temperature of 3606 K and concentration of 9.81E18 m^{-3}. Calculations were done at two pathlengths, 5 cm, the distance between the two windows in the optical path, and 1.2 cm, a closer approximation derived from a brief characterization of the plasma profile.

3.4 Tests Performed

A series of tests were performed to determine the variation in U I and U II transmission in environments with varying concentrations of O_2 mixtures with N_2 at 15 torr ambient pressure on a Uranium sample. Tests in an inert environment at varying pressures were performed on the same sample. Additional tests were performed at varying O_2/Ar mixtures, pressures, and laser powers to observe 593.55 nm UO band area trends. U_3Si_2 was also tested in a 2% O_2/98% Ar environment at varying spectral ranges to observe species of interest in post-nuclear event fractionation.

CHAPTER 4: RESULTS AND DISCUSSION

4.1 Changes in O_2 concentration

Three measurements each were taken at 5, 7, 9, 11, 13, and 15 μs after the onset of the plasma plume in environments of 10%, 20%, 30%, and 40% of O_2 and N_2 or Ar, as well as different concentrations of N_2 and Ar to rule out the possibility of nitride formation in this condition. Error bars shown are indicative of the standard deviation of the measurements taken per test condition. Figure 25 shows the temperatures calculated for U I and U II for each case tested.

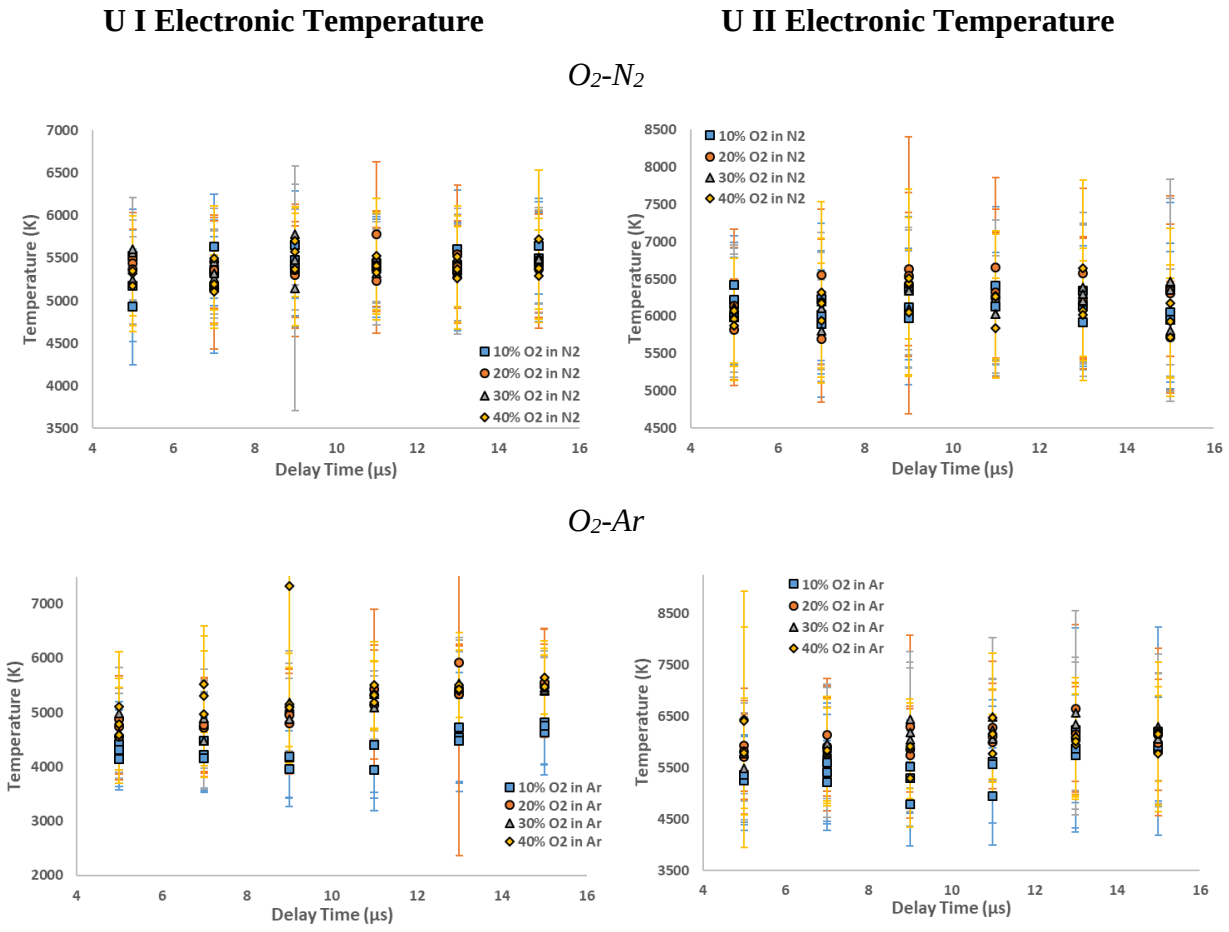

Figure 25: Calculated atomic temperatures for U I and U II.

N_2-Ar

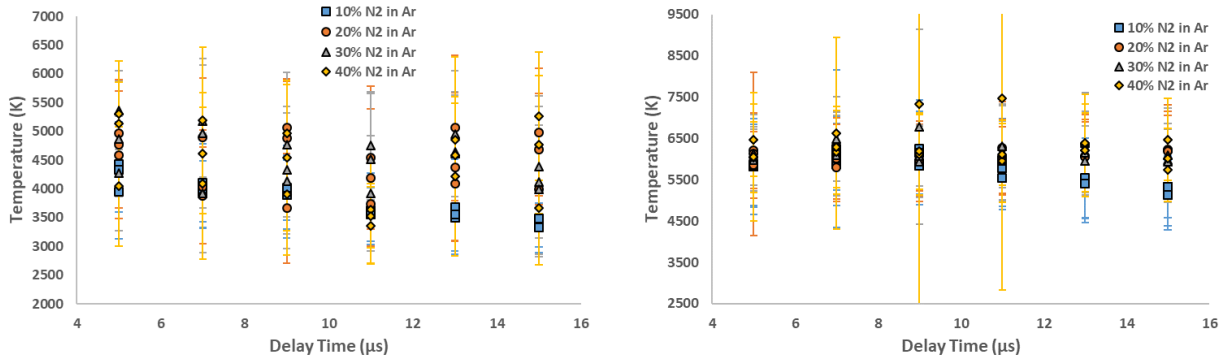

Figure 25 (cont.)

Temperatures were fairly constant for the delay times tested with some scatter likely due to the dynamic nature of the plume and fluctuation in power output from the Nd:YAG laser.

Figure 26 shows the calculated number density for the same tests. Note that the y-axis of the plots is scaled logarithmically.

U I Number Density **U II Number Density**

O_2-N_2

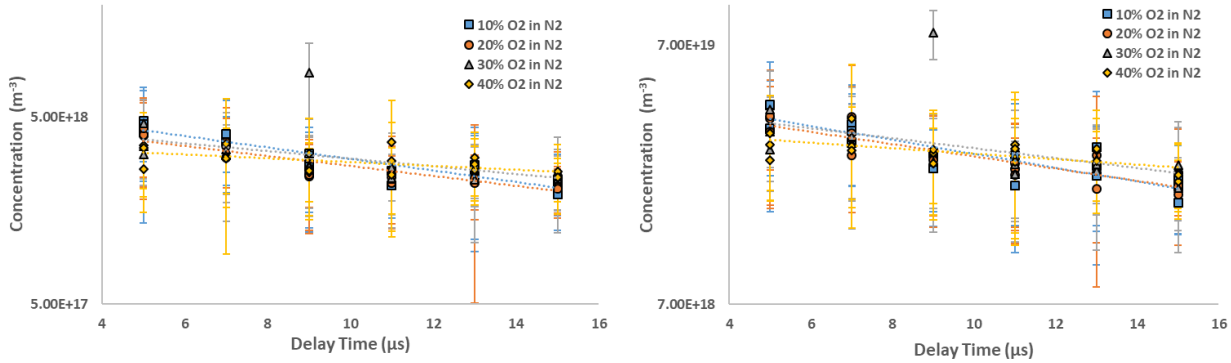

Figure 26: Number Densities of U I and U II calculated at estimated pathlength of 1.2 cm.

O_2-Ar

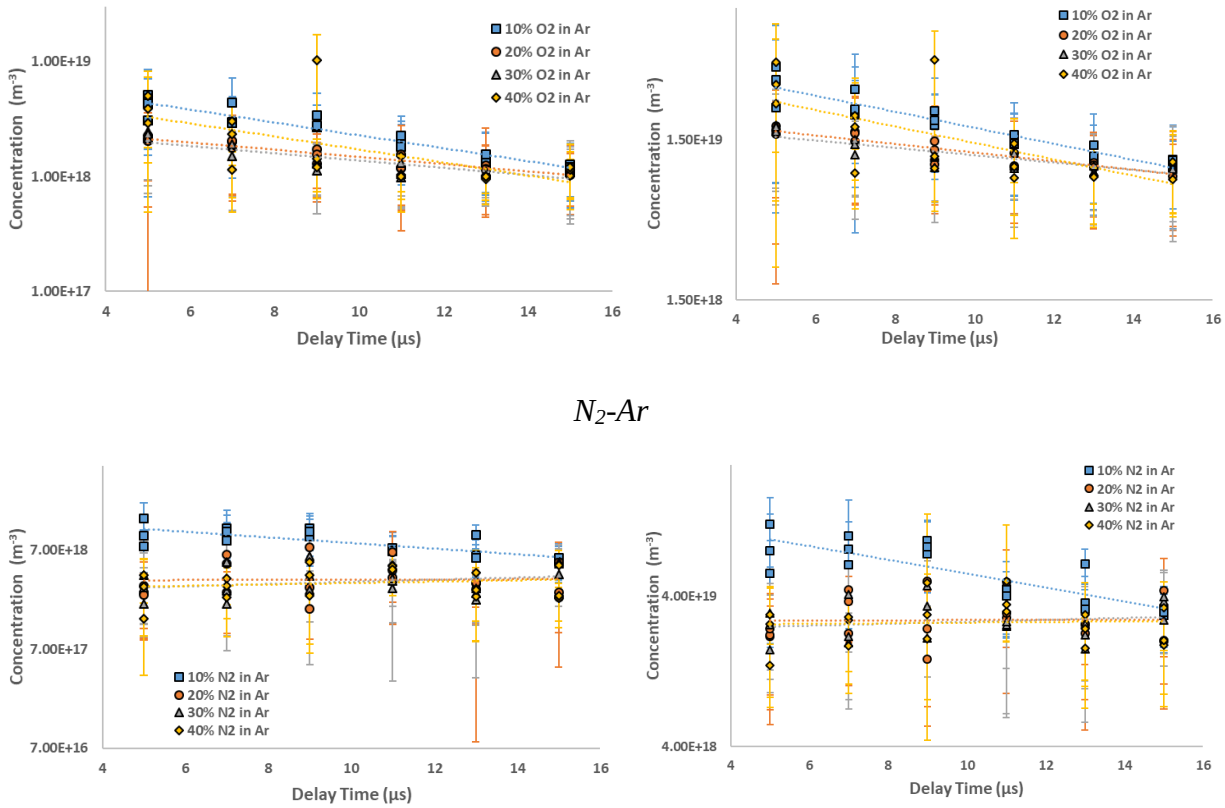

N_2-Ar

Figure 26 (cont.)

For the tests containing O_2 and N_2, there is a clear trend in decay constant (the negative slope of the lines plotted). The trend is less obvious for O_2 and Ar, while negligible decay is observed over this time period for environments containing mixtures of N_2 and Ar.

The time constants for each condition are plotted in Figure 27.

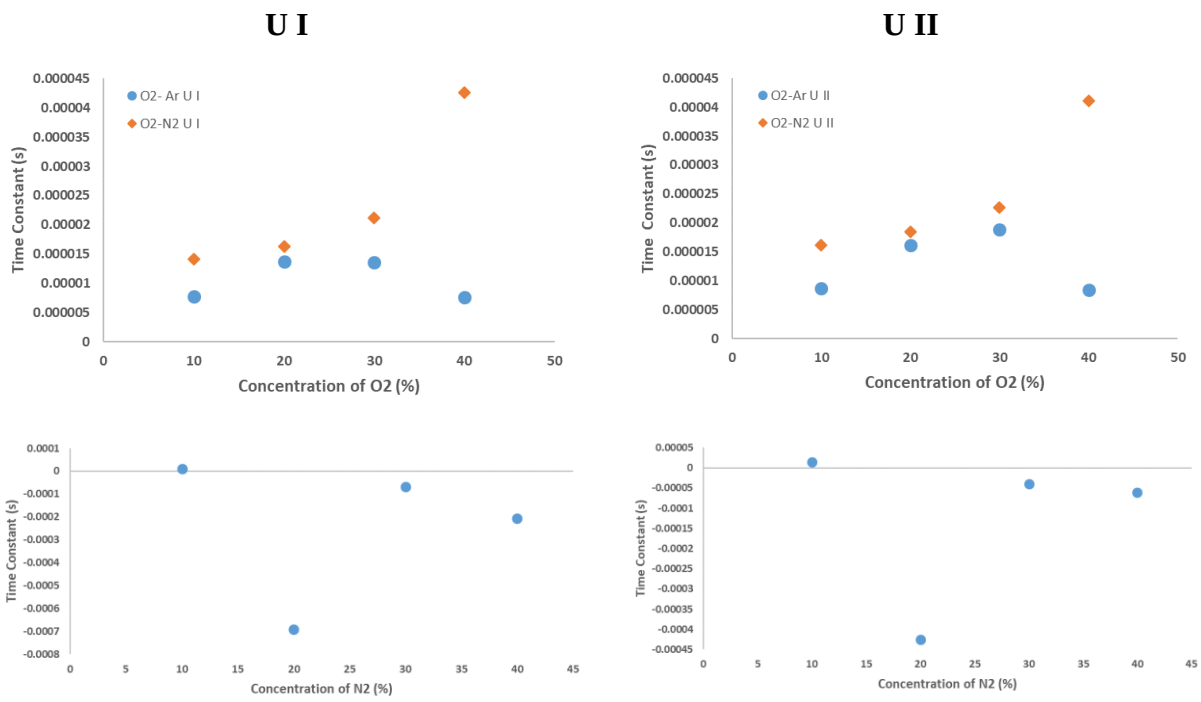

Figure 27: Time constants from exponential fits on number density data for U I and U II for all environment mixtures tested.

It was initially hypothesized that by monitoring the U I and U II formation, U oxidation could be gleaned by varying the O_2 concentration. This would indicate that the higher the amount of O_2 in the system, the faster individual U atoms form into oxides up to a certain point after which these atoms are poached by O atoms and combine into higher oxides. Prior methods of data processing supported this conclusion with large potential errors in calculation (exceedingly high standard deviation); however, when reprocessed using an amended method, deviations in calculated data were drastically reduced and the overall trends in data changed (See APPENDIX). Briefly, the old method of temperature and concentration calculation was based on the averaged spectrum from all 50 frames, whereas the new data processing scheme provides a temperature and concentration for each individual absorption frame and averages these values for each 50-frame shot.

The trend in time constants for both U I and U II for the mixtures containing O_2 is rather similar in that time constant increases with concentration of O_2 for O_2-N_2, and there is somewhat of a peak for the O_2-Ar mixtures, and no obvious trend for the inert mixtures (N_2-Ar) as would be expected. For the inert cases, the higher in magnitude and somewhat inconsistent trend in time constants indicate that the U atoms persist longer in that state due to the lack of oxygen for combination into

an oxide molecule. Thus, it does make sense that there might be some plateau as seen in the O_2-Ar time constants as there is a point where the atomic U ceases to form. However, it is unusual that the time constants increase with percentage of O_2 present because it was thought that higher amounts of ambient O_2 would encourage faster combination of U atoms into uranium oxides. This could be due to various factors. This diagnostic is location-dependent. All measurements taken for this series were in one location a few millimeters above the surface of the sample. Perhaps this location was not the primary site of UO or other oxide formation. As discussed in Section 2.1, the plasma plume is inhomogeneous; therefore, perhaps a region with a higher concentration of atomic U is being probed. The plasma plume is dynamic and is subject to other factors as well. Temperature varied frame-by-frame as did concentration of atomic U species. The standard deviations are indicated by error bars in Figure 25 and Figure 26. These combined factors indicate that indirectly observing oxide formation may not be the best approach.

4.2 Observation of UO

Fortunately, oxides can be observed directly using absorption spectroscopy under the right conditions. The UO 593.55 nm and 594.57 nm bands were observed in transmission and various trends in band area were tracked. Future work will be done to quantify concentration, but trends in band area are analogous and therefore worthwhile to report. That having been said, this assumption suffers from lack of knowledge about the temperatures at which these bands are sensitive to change. Although some work has been done in quantifying molecular formation of uranium oxides, information remains incomplete [20], [24]. Figure 28 shows the two UO bands observed.

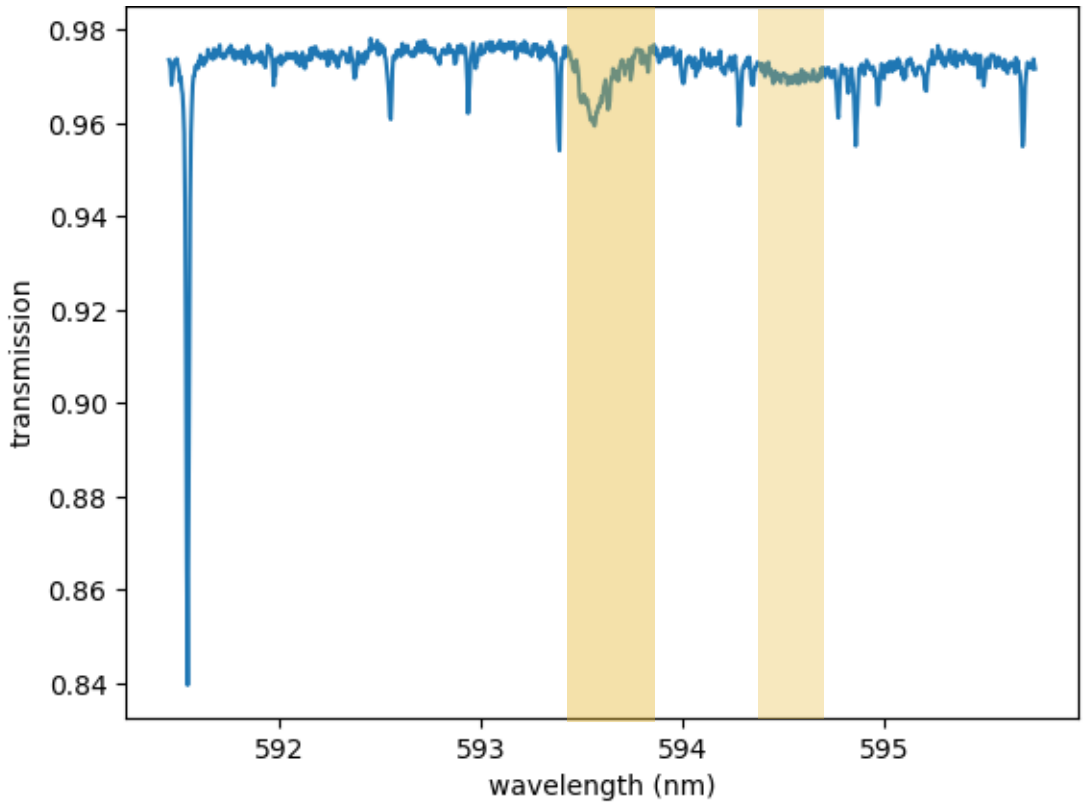

Figure 28: Spectrum of ablated U plasma in the 591-596 nm region, taken at 5 μs delay.

When tracked against each other, the 594.57 nm band area proved to remain about 1.5x less the magnitude of the 593.55 nm band area consistently, thus only trends in the 593.55 nm band will be reported here.

Figure 29 shows band area trends over delay time for various concentrations of O_2 in Argon environment at a fixed pressure of 15 torr. In general, it appears that band area is higher overall at lower concentrations of O_2 in Argon.

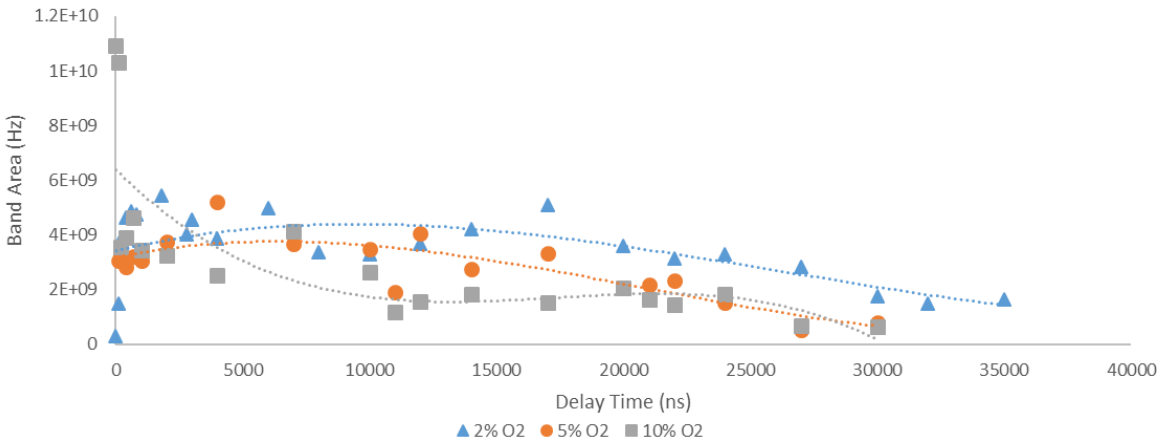

Figure 29: Area of 593.55 nm band versus delay time for different concentrations of ambient O_2 in Ar.

Perhaps higher ambient O_2 concentration hastens the transition of UO into higher oxides. However, it is difficult to ascertain this trend without quantitative data.

Figure 30 shows trends in band area for a 10% O_2/90% Ar environment with changes in ambient pressure.

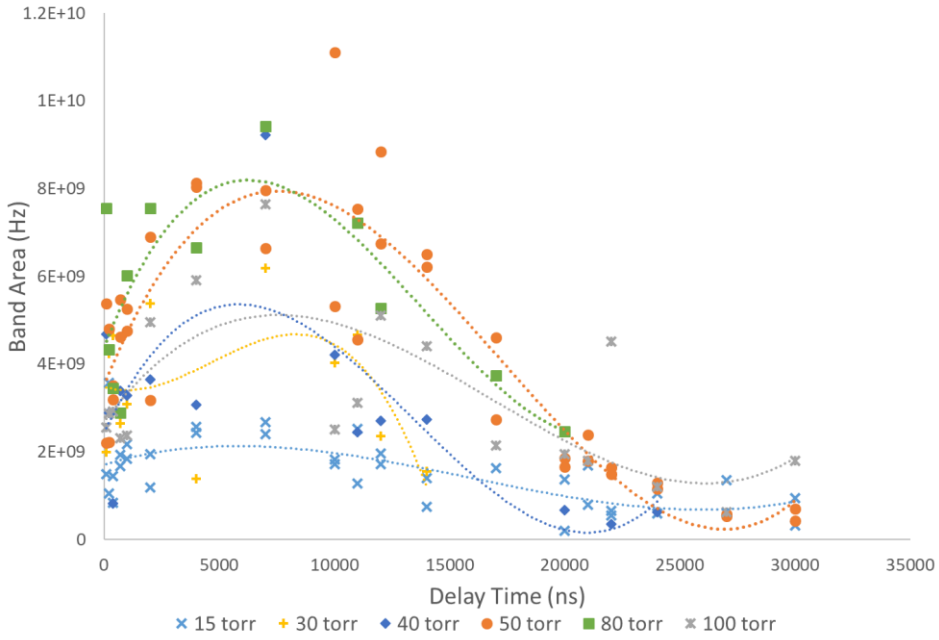

Figure 30: Area of 593.55 nm band versus delay time for uranium ablation in 10% O_2/90% Ar at various pressures.

From these results, it can be determined that there is somewhat of a peak in band area in between 50 and 80 torr. This trend is somewhat unusual and further work will be done to characterize and reproduce this result. This could also be due to spatial factors since the plume size varies with changes in pressure and UO may be forming in a different part of the plume. All measurements were taken in the same spot, so changes in concentration may be partially due to movement of constituents in an inhomogeneous plume as opposed to actual change overall in UO concentration.

Figure 31 is an alternate representation of some of the information shown in Figure 30. Instead of tracking the band area across time, band area is tracked across various pressures at a few instances in time.

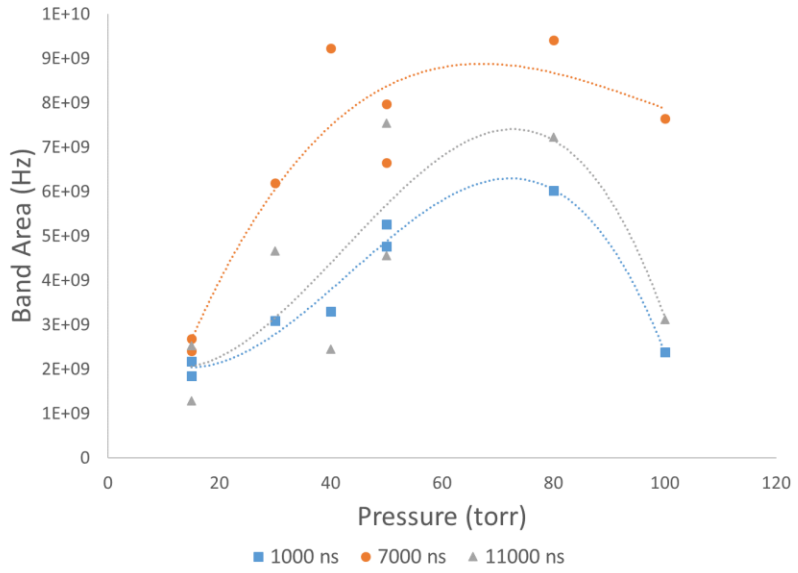

Figure 31: 593.55 nm band area tracked across varying pressures for a given delay time in a 10% O_2 environment.

This highlights the existence of a 'peak' band area around 70 torr ambient pressure that ought to be studied further. As mentioned earlier, spatial variations can contribute to band area trends. Figure 32 shows trends with respect to time for various locations above the sample in 100 torr ambient pressure.

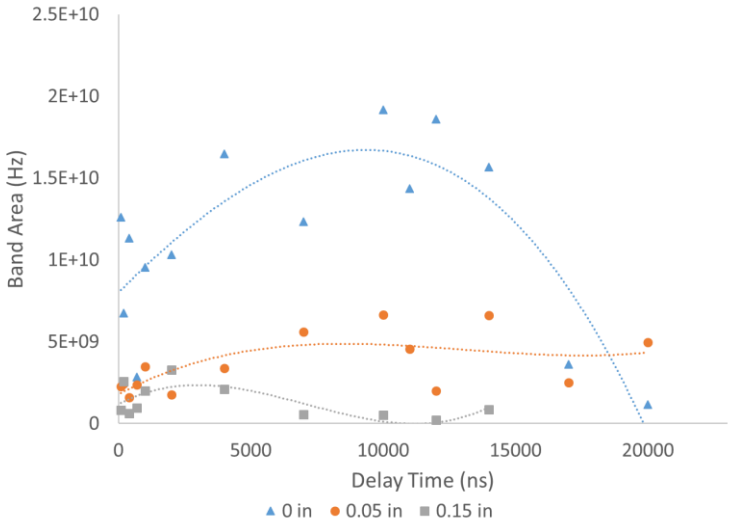

Figure 32: Area of 593.55 nm band in 100 torr, 2% O_2 for various positions.

As would be expected, there is a higher concentration of UO overall closer to the sample itself. However, the trends in band area over time for each location are quite different, which further underscores inhomogeneity of the plasma plume. Further work will be performed in the future to characterize the spatial distribution of the various constituents.

Additionally explored was the dependence of band area on laser power per pulse, which does fluctuate. Figure 33 shows this relationship.

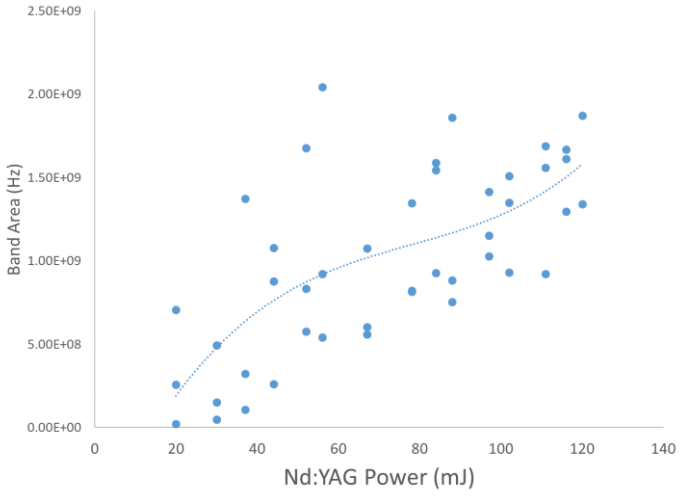

Figure 33: Area of 593.55 nm band in 15 torr, 2% O_2 environment versus Nd:YAG power output. Note the general upward trend, with large fluctuation.

Although there is considerable scatter, there is a general upward trend in band area with laser power. Laser power is monitored during testing to ensure that it is as close to constant as possible in order to reduce this scatter, but fluctuations occur nonetheless.

4.3 U_3Si_2 Features Observed

A sample of U_3Si_2 was ablated in order to determine the spectral signatures of certain constituents that might be present after a nuclear detonation event and their temporal evolution. Figures 34-37 show how the transmission spectra for various delay times from ablation pulse for SiO, Si I, U I and U II, and UO respectively.

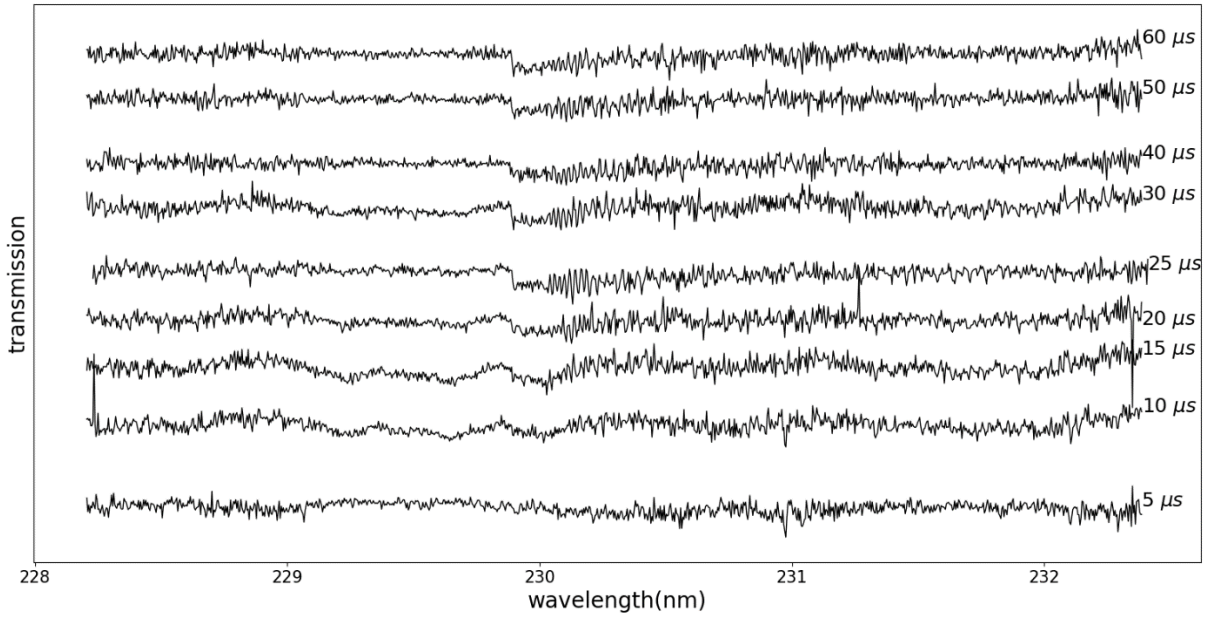

Figure 34: Time-resolved SiO band transmission spectra.

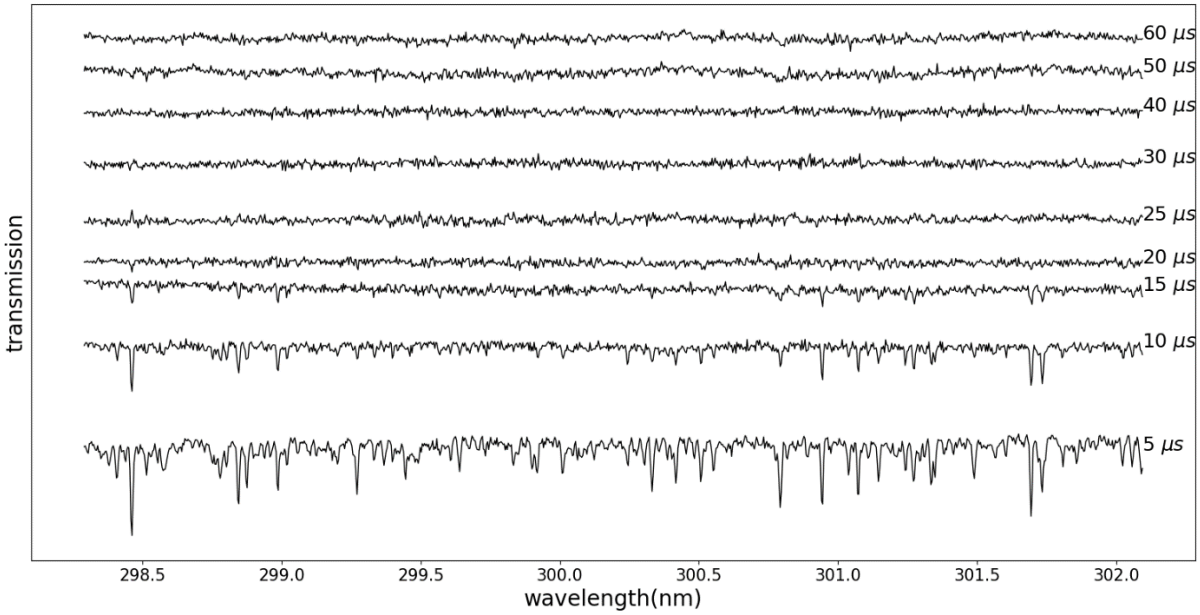

Figure 35: Time-resolved transmission spectra used for atomic Si I temperature and concentration calculation. Note that most of these peaks actually belong to Uranium species.

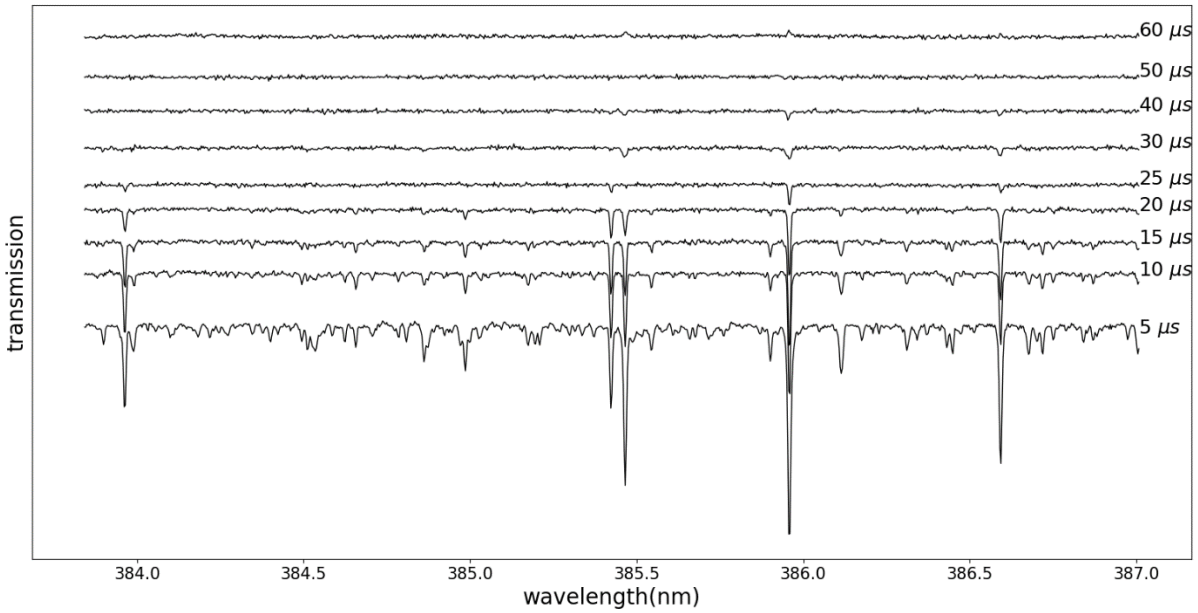

Figure 36: Time-resolved transmission spectra used for U I and U II temperature and concentration calculation.

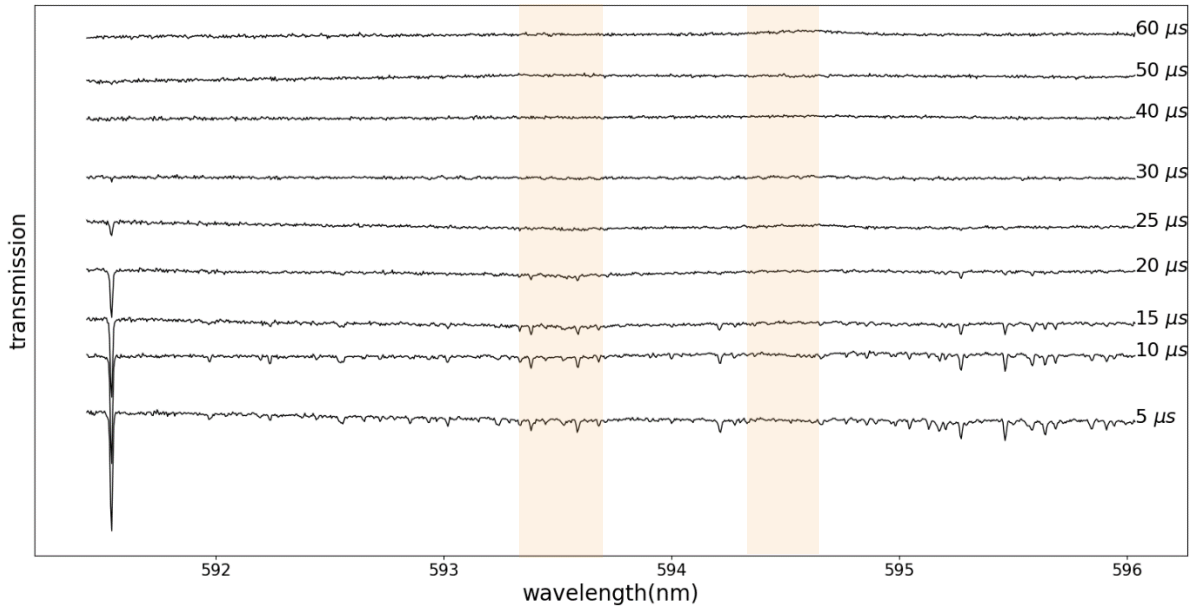

Figure 37: Time-resolved UO transmission spectra. Band locations are highlighted.

From these spectra, it can be determined that the SiO band targeted forms slightly later and persists significantly longer than the signal from the other species observed. The atomic transitions and the UO band signal faded before the 30 μs point for the most part.

Figure 38 and Figure 39 show trends in the available temperatures and concentrations for the species observed. Unfortunately, UO temperature and concentration and SiO concentration could not be determined for this work. Further work will be done to determine that information, as well as improve upon the SiO model to calculate more accurate temperatures.

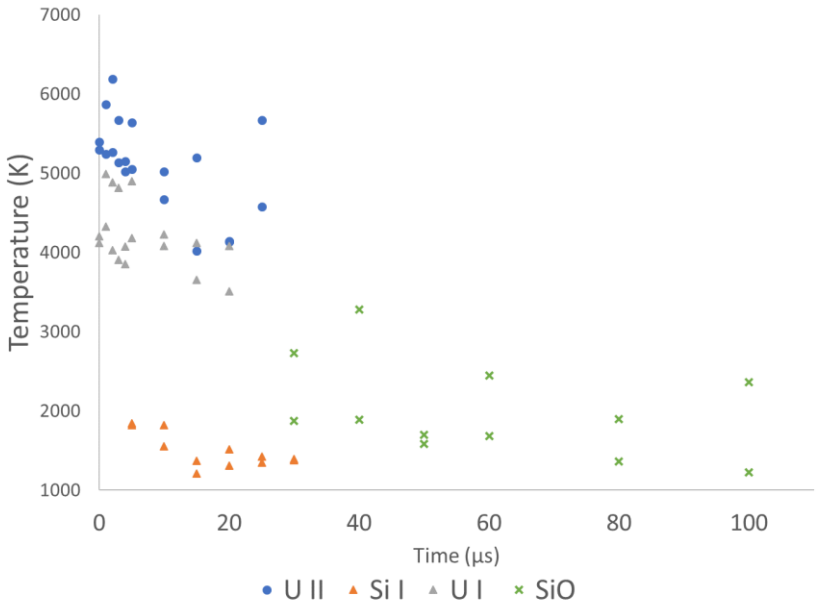

Figure 38: Temperatures versus time for observed species.

In general, temperatures decreased over time for the species studied. Due to having fewer lines and weaker transitions (detailed in section 2.4) comparatively to the atomic U signatures, calculated Si I temperatures and concentrations may be more prone to error.

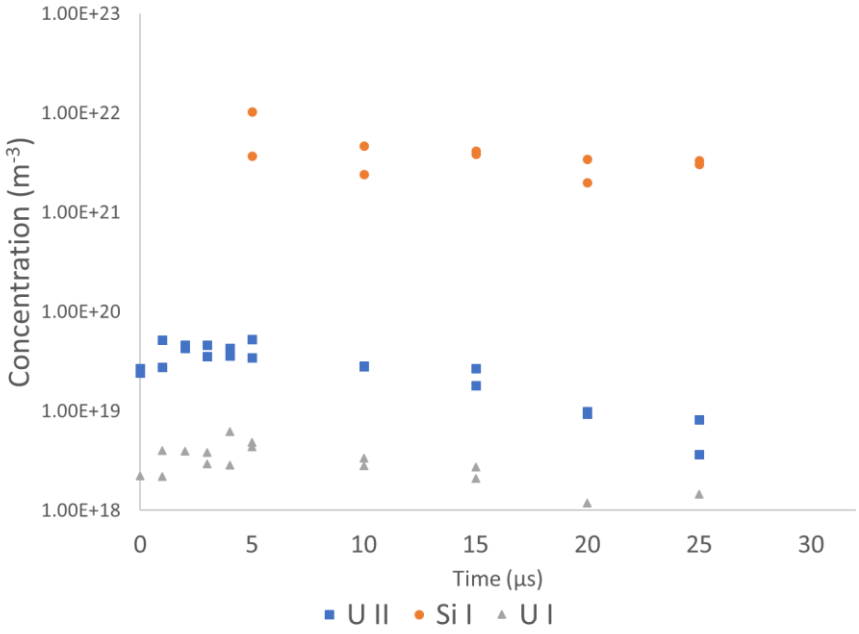

Figure 39: Calculated concentrations for atomic species.

4.4 Uncertainty Analysis

For all the work previously discussed, individual data points corresponded to measurements averaged across 50 emission spectra and 50 spectra where absorption was taking place in order to account for the dynamicity of the plume between pulses. Within those 50 spectra, temperature, concentration, and signal quality can vary. The following figures show U I temperature and concentration data obtained from a few tests in the 382-385 nm region, at 5 μs, 7 μs, and 9 μs (Figure 40, Figure 41). The horizontal dotted lines represent the mean temperatures and concentrations calculated from the individual frames, and the dashed lines represented the curve of growth correction based on calculations on the averaged spectrum. It was impractical to perform curve of growth calculations on the individual spectra due to the amount of time required for the iterative process through which curve of growth corrections are obtained.

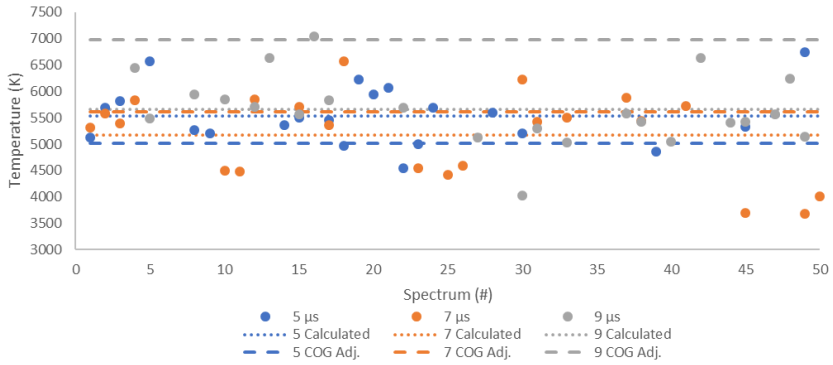

Figure 40: Temperature of U I in 382-385 nm range for each frame in a single measurement for 5 μs, 7 μs, and 9 μs, plotted against overall mean temperatures, and curve of growth adjusted temperatures.

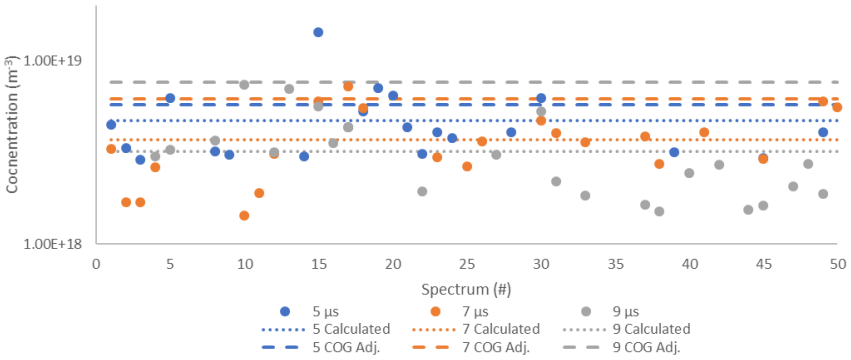

Figure 41: Concentration of U I in 382-385 nm range for each frame in a single measurement for 5 µs, 7 µs, and 9 µs, plotted against overall mean concentrations, and curve of growth adjusted concentrations.

When observed frame-by-frame, there is considerable scatter in both the temperature and concentration data. This could vary based on signal quality, as mentioned earlier, and which transitions are being used for the calculation, as it is unlikely that temperature was fluctuating thousands of degrees on such a short timescale. Or, the plume could be incredibly turbulent. Figure 42 shows the r-values for the Boltzmann plots used to determine temperature for each frame.

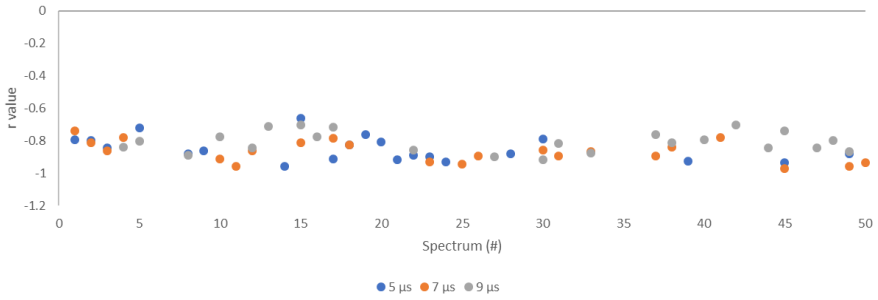

Figure 42: R-values for Boltzmann plots for each frame for U I in 382-385 nm range.

For the most part, the r-values for this range are reasonable as spectra that fail to yield valid temperature and concentration measurement are parsed out from the mean temperature and concentration calculation. That having been said, utilizing the Boltzmann distribution for temperature calculation requires the assumption that the system is in equilibrium, which it may not be, and may also account for deviations.

Figures 43-45 show the same plots for U II calculations in the same range.

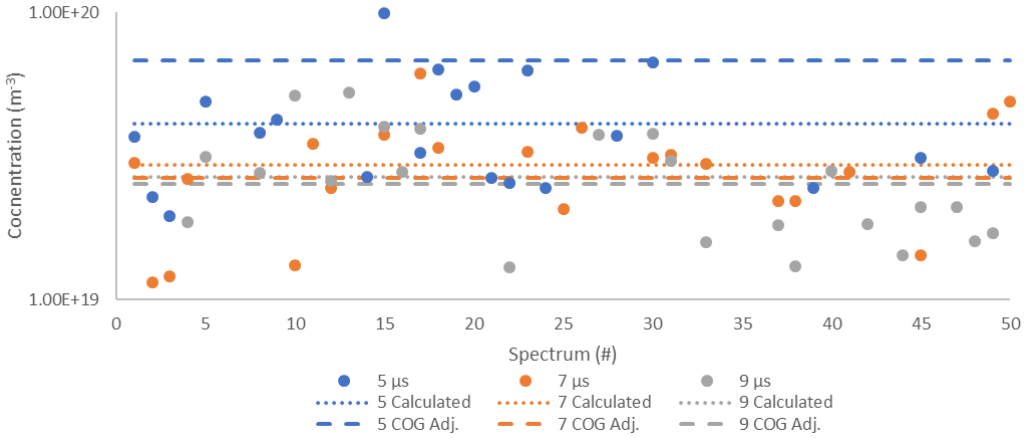

Figure 43: Concentration of U II in 382-385 nm range for each frame in a single measurement for 5 µs, 7 µs, and 9 µs, plotted against overall mean concentrations, and curve of growth adjusted concentrations.

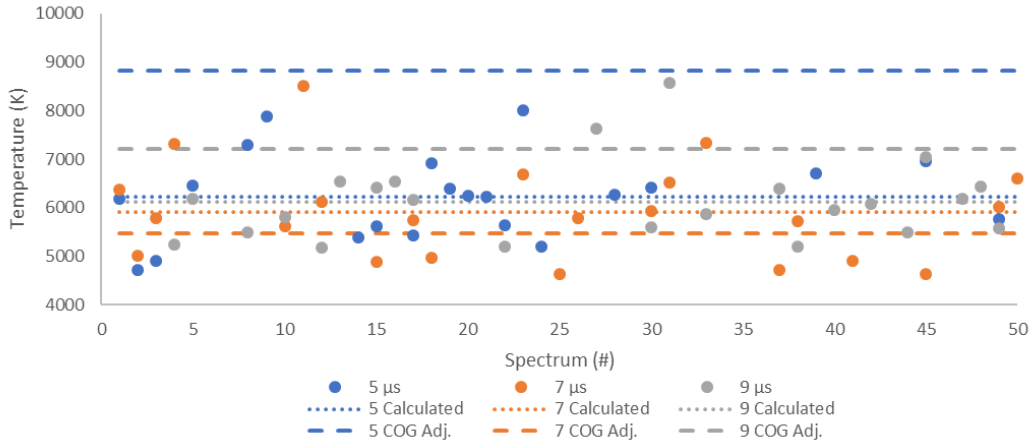

Figure 44: Temperature of U II in 382-385 nm range for each frame in a single measurement for 5 µs, 7 µs, and 9 µs, plotted against overall mean temperatures, and curve of growth adjusted temperatures.

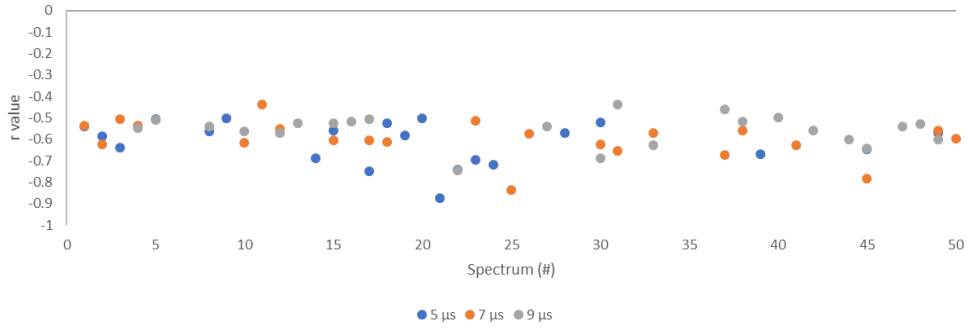

Figure 45: R-values for Boltzmann plots for each frame for U II in 382-385 nm range.

As mentioned earlier, the distribution and r-values can vary greatly with the transitions used to calculate temperature and concentration. It is clear that the Boltzmann agreement is worse for U II from Figure 45. Across the board, there is an improvement in accuracy from previous temperature calculation methods involving the averaged spectrum. Calculating temperature with the averaged spectrum artificially lowers the temperature output as it includes frames that sometimes do not include spectra at all.

CHAPTER 5: CONCLUSIONS AND RECOMMENDATIONS

5.1 Summary and Conclusions

A sample of U was ablated and spectroscopically characterized to determine changes in spectral signature under various environmental conditions. The persistence of U I and U II transitions was tracked over differing concentrations of O_2, indicating that at higher oxygen concentrations, atomic U forms into oxides more quickly. The 593.55 and 594.57 nm bands of UO were observed in transmission under various pressures, locations, laser powers, and ambient concentrations of O_2. An attempt was made to observe uranium nitride formation, which proved ineffective.

A sample of U_3Si_2 was studied to determine how U behaves in the presence of Si, one of the most commonly found elements, and very likely to be found in nuclear debris. Time-resolved spectral measurements were taken of SiO, Si I, U I, U II, and UO in transmission. It was found that all atomic species and UO developed earlier in time, consistent with previous results in the pure U sample, but SiO band developed much later in time around the 30 μs mark. Temperatures and concentrations for atomic species were also calculated.

5.2 Plans and Recommendations for Future Work

Further work will be done to calculate the concentrations of SiO and UO.

Work will be done to develop a more robust and versatile suite of code in Python to process LIBS data, with changes made to improve calculation accuracy and remove outliers due to bad signal. These changes include the development of an algorithm to sort out spectra with bad signal and modules to readily access and output information such as transmission and absorption spectra, temperatures and concentrations of constituents, and frame-by-frame breakdown of calculations to ensure removal of outlier spectra that can be easily adjusted for use with various species in various spectral locations.

Dr. Glumac made a new chamber in order to achieve a lower vacuum environment which possesses capability for imaging and ease of vertical and horizontal translation for spatial characterization of the laser-induced plume. Work will be done to validate that results produced are similar to that of the old chamber, prior to proceeding with future tests.

Shock tube testing will be performed to observe spectral changes in combustion of uranium at various, highly-controllable temperatures. LIBS will also be attempted on the pure U sample with various methods to change plasma temperature, as well as at different pressures to determine these changes.

Other actinide materials and alloys will be subjected to a similar testing scheme and their signatures catalogued to further build the base of information on actinide materials, as well as assist in the calibration of models in development.

REFERENCES

[1] N. M. Laurendeau, *Statistical Thermodynamics, Fundamentals and Applications*. 2005.

[2] D. Curreli, "DTRA Basic Research Annual Report," 2017.

[3] M. S. Finko *et al.*, "A model of early formation of uranium molecular oxides in laser-ablated plasmas," *J. Phys. D. Appl. Phys.*, vol. 50, no. 48, 2017.

[4] M. DeMagistris, N. Sinha, E. Weerakkody, N. Falcone, and J. Lightstone, "2018 Annual Report HDTRA1-17-1-0026." Combustion Research and Flow Technology Inc., 2018.

[5] J. T. Verdeyen, *Laser Electronics*. Englewood Cliffs, NJ: Prentice-Hall, Inc., 1981.

[6] "Synopsis of Spectroscopic Measurements," *NPTEL*, 2013. [Online]. Available: https://nptel.ac.in/courses/102103044/3.

[7] J. Hermann, F. Coursimault, O. Motret, S. Acquaviva, and A. Perrone, "Investigation of silicon oxide emission spectra observed in a pulsed discharge and a laser-induced plasma," vol. 4075, no. 01, pp. 1917–1927, 2001.

[8] K. P. Huber and G. Herzberg, "Constants of Diatomic Molecules," *NIST Chemistry WebBook, NIST Standard Reference Database Number 69*. .

[9] C. M. Western and B. E. Billinghurst, "PGOPHER, A Program for Simulating Rotational, Vibrational and Electronic Spectra." University of Bristol Research Data Repository, 2017.

[10] N. Glumac, G. Elliott, and M. Boguszko, "Temporal and Spatial Evolution of the Thermal Structure of a Laser Spark in Air."

[11] T. Ida, M. Ando, and H. Toraya, "Extended pseudo-Voigt function for approximating the Voigt profile," *J. Appl. Crystallogr.*, vol. 33, no. 6, pp. 1311–1316, 2000.

[12] D. W. Hahn and N. Omenetto, "Laser-induced breakdown spectroscopy (LIBS), part II: Review of instrumental and methodological approaches to material analysis and applications to different fields," *Applied Spectroscopy*. 2012.

[13] D. A. Cremers and L. J. Radziemski, *History and fundamentals of LIBS*, vol. 9780521852. 2006.

[14] Q. L. Ma *et al.*, "Temporal and spatial dynamics of laser-induced aluminum plasma in argon background at atmospheric pressure: Interplay with the ambient gas," *Spectrochim. Acta - Part B At. Spectrosc.*, 2010.

[15] V. I. Babushok, F. C. DeLucia, P. J. Dagdigian, M. J. Nusca, and A. W. Miziolek, "Kinetic modeling of the laser-induced breakdown spectroscopy plume from metallic lead.," *Appl. Opt.*, vol. 42, no. 30, pp. 5947–62, 2003.

[16] R. . Gleason and D. . Hahn, "The effects of oxygen on the detection of mercury using laser-induced breakdown spectroscopy," *Spectrochim. Acta Part B At. Spectrosc.*, vol. 56, no. 4, pp. 419–430, 2001.

[17] P. J. Skrodzki *et al.*, "Significance of ambient conditions in uranium absorption and emission features of laser ablation plasmas," *Spectrochim. Acta - Part B At. Spectrosc.*, vol. 125, pp. 112–119, 2016.

[18] Zhang, D. Zhang, X. Ma, S. Wang, X. Zhu, and Zhang, "Influence of Ambient Gas on Laser-Induced Breakdown Spectroscopy of Uranium Metal," *Plasma Sci. Technol*, vol. 17, 2015.

[19] S. S. Harilal, P. K. Diwakar, N. L. Lahaye, and M. C. Phillips, "Spatio-temporal evolution of uranium emission in laser-produced plasmas," *Spectrochim. Acta - Part B At. Spectrosc.*, 2015.

[20] S. S. Harilal, B. E. Rumfield, N. G. Glumac, and M. C. Phillips, "Elucidating uranium monoxide spectral features from a laser-produced plasma," *Opt. Express*, vol. 26, no. 16, pp. 54–62, 2018.

[21] M. Miyabe *et al.*, "Ablation plume structure and dynamics in ambient gas observed by laser-induced fluorescence imaging spectroscopy," *Spectrochim. Acta - Part B At. Spectrosc.*, vol. 110, pp. 101–117, 2015.

[22] R. Noll, *Laser-Induced Breakdown Spectroscopy: Fundamentals and Applications*. Heidelberg: Springer-Verlag Berlin Heidelberg, 2012.

[23] D. J. Matthew and M. D. Morse, "Resonant two-photon ionization spectroscopy of jet-

cooled UN: Determination of the ground state," *J. Chem. Phys.*, vol. 138, no. 18, 2013.

[24] X. Mao, G. C. Y. Chan, I. Choi, V. Zorba, and R. E. Russo, "Combination of atomic lines and molecular bands for uranium optical isotopic analysis in laser induced plasma spectrometry," *J. Radioanal. Nucl. Chem.*, vol. 312, no. 1, pp. 121–131, 2017.

[25] L. A. Kaledin, J. E. McCord, and M. C. Heaven, "Laser spectroscopy of UO: Characterization and assignment of states in the 0- to 3-ev range, with a comparison to the electronic structure of ThO," *Journal of Molecular Spectroscopy*, vol. 164, no. 1. pp. 27–65, 1994.

[26] P. L. Smith, C. Heise, J. R. Esmon, and R. L. Kurucz, "Division of Plasmaphysics - Atomic spectral line database," *Hannover University*, 2018. [Online]. Available: http://www.pmp.uni-hannover.de/cgi-bin/ssi/test/kurucz/sekur.html.

[27] "Using Radioactive Materials," *Division of Research Safety*, 2017. [Online]. Available: http://www.drs.illinois.edu/Programs/LaboratoryPrecautions.

[28] "Compressed Gas Cylinder Safety," *Division of Research Safety*, 2018. [Online]. Available: http://www.drs.illinois.edu/SafetyLibrary/CompressedGasCylinderSafety.

[29] "Python Language Reference." Python Software Foundation.

APPENDIX

Absorption LIBS Temperature/Concentration Calculation Pseudocode

Main Module

1. Selects directory for operation and specifies which files to tabulate information from.
2. Calls module separate dark, source, LIBS + source, and emission spectra given data files.
    a. Separate modules for Hamamatsu and Andor files
3. "Absorption" object is created from the separated data and calibration information.
    a. Contains: wavelengths, frequencies, wavenumbers, transmission, absorption, and information necessary to calculate equivalent width
4. Vectors of temperatures, concentrations, and r-values are made by iteration through all 50 transmission spectra for one shot. A file containing these is outputted for each species tested.
5. Overall temperature for averaged spectrum is calculated as well as r-value, concentration, and curve-of-growth corrected concentration and temperature. The mean temperature, concentration, and standard deviations from all 50 spectra are also output. A file summarizing these for a test series is also output.

Temperature Module

1. "Energy State Information" object is created to obtain wavelengths, Blu, lower energy states, and other parameters from an input file.
2. A check is run to double-check that the transitions observed are within the range of wavelengths that the data is calibrated for.
3. Peak areas for transitions observed are obtained from the peak area search function.
4. The spread of the lower energy levels for the peaks that do appear is checked (i.e. if they are sensitive to the appropriate temperature range). If these values are not sufficiently far apart, a temperature cannot be calculated and the function outputs 'NaN'.
5. If the previous check clears and there are more than 2 peaks present, ln (W_{lu}* v/(B_{lu}* gl)) and lower energy states are regressed to obtain temperature.
    a. If a temperature comes out negative for whatever reason (usually not enough peaks are present), the value is thrown out and the function outputs 'NaN' for both temperature and r-value.
    b. Otherwise, temperature and r-value for Boltzmann regression are output from the function.

Peak Area search function

1. The ideal transition wavelengths from Kurucz and calibration absorption data are fed in this function
2. The function finds all peaks in the absorption data.

3. For each peak, bounds are found for peak area integration. Equivalent widths are also calculated.
4. The function searches through the indices of the calibrated data to find the peaks occurring at that wavelength within a small berth.
5. If the transition does not appear, the peak area value is set to 0.
6. Relevant equivalent widths, peak areas, and transitions that were actually observed are output.

Concentration Module

1. Takes temperature input, "Energy state information" object, "absorption" object, pathlength, energy state filename
2. Checks if the temperature input is greater than 0
    a. Makes sure that it's not a 'NaN' and that code was not input improperly.
3. Calculates the populations at each energy state, n_i = peak area/h/ν/B_{lu}/L
4. Gets partition function value from separate function given temperature and location of data.
5. Back calculates for concentration from each transition and averages the obtained values.

Concentration Module with Curve of Growth Module

1. Operates much the same as the regular concentration module, except that equivalent widths and temperature are worked into a curve of growth adjustment and then concentration is calculated.
2. Adjusted temperature, concentration, and r-values are output.

Partition Function module

1. Calculates partition function given temperature and a file containing an array of lower energy states and J terms.

Changes from Previous iteration of code:

1. Curve of growth is implemented for averaged spectrum but not for individual spectra (time for computation would be way too high).
2. There is improved baseline subtraction from transmission data (i.e. continuum is removed)
3. Temperatures and concentrations are obtained from individual transmission spectra and averaged.
    a. This leads to higher temperatures overall because averaging in the spectra where 'nothing' occurred reduced the temperatures.

Overall, there are more checkpoints to prevent things from going wrong with the code (i.e. if statements to make sure that temperature values are positive).